Probing the interstellar medium of high-redshift sub-millimetre and emission line galaxies

by

Daniel J. M. Cunningham

A Thesis Submitted to Saint Mary's University, Halifax, Nova Scotia in Partial Fulfillment of the Requirements for the Degree of Master of Science in Astronomy (Department of Astronomy and Physics)

August 2018, Halifax, Nova Scotia

Approved: Dr. Scott Chapman

Supervisor

Approved: Dr. Rob Thacker

Co-supervisor

Approved: Dr. Ivana Damjanov

Committee Member

Approved: Dr. Marcin Sawicki

Committee Member

Date: August 24, 2018

Acknowledgements

First and foremost, I would like to thank my supervisor Scott Chapman for being an endless resource of help. He was often available at all hours of the night, and all hours of the morning during ALMA proposal deadlines. He provided me with opportunities to study parts of the universe I am most interested in and to use some of the world's most advanced observatories.

I would also like to thank the South Pole Telescope Sub-Millimeter Galaxies collaboration, specifically Carlos De Breuck, Joaquin Vieira, and Justin Spilker who provided substantial help and criticism that is necessary for any scientist to grow.

Finally, I would like to thank the students and faculty at Saint Mary's University for giving me an excellent two years of studying the universe.

Contents

List of Figures

List of Tables

Abstract

Probing the interstellar medium of high-redshift sub-millimetre and emission line galaxies

by Daniel J. M. Cunningham

Utilizing new ALMA-ACA observations of the [N II] 205 μm line in combination with existing [C II] 158 μm observations, we characterize the $L_{[C\ II]}/L_{[N\ II]}$ distribution in high-redshift sub-millimetre galaxies. Our measurements are consistent with existing literature of high-redshift $L_{[C\ II]}/L_{[N\ II]}$. Compared to local (U)LIRGs, our measurements find higher luminosity ratios which indicates a key difference in physical parameters of the interstellar medium. We also present the first stages of a wide-field narrow-band emission line survey using CFHT WIRCam, including details of its initial success.

August 24, 2018

Chapter 1

Introduction

The universe is by all measures almost completely empty and dark, but at the same time it is full of incomprehensibly massive and luminous things. These things come in many forms such as active galactic nuclei, blackholes, bright O and B type stars, and galaxies. Galaxies are one of the most important things for us to study since they are the cosmic homes of matter we can see like stars, gas, and dust. They also contain matter we cannot see directly (yet – perhaps technological advancements will allow us to) like dark matter and blackholes. Galaxies come in different shapes and sizes, some earning the name "dwarf galaxy" for their relatively small size and low mass, or "elliptical galaxy" because of their elliptical shape. Other galaxies may earn their names based on the radiation they emit, such as a "sub-millimetre galaxy" (SMG). These galaxies earned their name by emitting a significant fraction of their energy at sub-millimetre wavelengths. They are massive galaxies, many of which formed early in the history of the universe. Many of them host some of the most rapid star formation ever observed, but because of their high dust content they can

be difficult to study at optical and ultraviolet wavelengths. The following sections discuss methods to study these galaxies in addition to some characteristics common to all galaxies.

1.1 Overview of galaxies

Observational astronomers study galaxies by observing the electromagnetic radiation they emit and how they interact with their surroundings. Their spectrum—which is affected by emission and absorption of light by gas, and dust—can provide information regarding their composition, interstellar medium, stellar populations, and whether it is actively forming new stars. Radiation emitted by stars is one of the most important things to observe when studying galaxies, and it can shed light on the age of a galaxy's stellar population. For instance, young and massive stars have extremely high surface temperatures of > 20000 K, but have short lives compared to lower mass stars like our sun. This is the result of their enormous energy output, which depletes their fuel at a faster rate compared to less massive stars. These young and massive stars, called O and B type stars, are more luminous and have a spectral energy distribution (SED) concentrated at higher frequencies compared to lower mass stars on the main sequence. This behaviour can be understood using Planck's Law shown below:

$$B_\nu(\nu, T) = \frac{2h\nu^3}{c^2} \frac{1}{e^{\frac{h\nu}{kT}} - 1} \tag{1.1}$$

In Planck's Law, since higher temperatures (T) decrease the exponent of $e^{\frac{h\nu}{kT}}$, the denominator will decrease, therefore increasing the SED amplitude at a set frequency (ν).

Where this peak in energy occurs depends on how large the numerator of this $e^{\frac{h\nu}{kT}}$ term is, in addition to the temperature. Here h is Planck's constant, k is the Boltzmann constant, and c is the speed of light.

Equation 1.1 demonstrates that because of the high surface temperatures of O and B type stars, they emit primarily at ultraviolet and optical wavelengths ($\sim 10^{-6}$ to 10^{-8} m). An actively star-forming galaxy should have a significant component of their integrated light at ultraviolet and optical wavelengths if the light escapes the galaxy without being absorbed or scattered. These galaxies will naturally appear more "blue" because of the higher frequency light in their SEDs. In galaxies without significant active star formation, or with old stellar populations—where the young and hot stars have died off—the emitted light will appear more "red".

However, in galaxies where star-forming regions are embedded within high concentrations of dust, as is the case in SMGs, ultraviolet and optical photons are likely obscured and absorbed by dust (Calzetti et al. 2000; Blain et al. 2002; Draine 2003). After absorbing these photons, the dust grains re-emit the light at longer wavelengths through thermal emission. In sub-millimetre galaxies, this thermal emission is a dominant feature of their SED which helps explain why they remained undetected until the 1990s, after hundreds of years of astronomical research at optical wavelengths.

1.2 Understanding SMGs and their evolution

Understanding galaxy populations is a difficult endeavour. Different types of galaxies have different properties. In many cases they are different enough that they must be observed using separate regions of the electromagnetic spectrum. Furthermore, different types of galaxies may evolve in different ways and appear to be a distinct type of galaxy in earlier epochs of cosmic time. Galaxy sizes, star formation rates, and spectral energy distributions may all change. Since the timescale for galaxy evolution is so long, observations of the universe only capture a snapshot of these populations which astronomers must assemble to tell the story of galaxy evolution.

Early astronomers like Max Wolf and Knut Lundmark used photography to study galaxies, but were limited to studying them according to their appearance in optical light at wavelengths of approximately 400 to 800 nm (Conselice 2014). These photographs and the common appearances of galaxies in them developed into what is now called the Hubble Classification or Hubble Tuning Fork. While it is understood that the Hubble Classification does not represent a true evolutionary sequence, it still helps illustrate key differences among common galaxies in the universe. It is separated into three main components: the elliptical galaxies, the spiral galaxies, and the barred spiral galaxies.

Elliptical galaxies are important to understand, as they may be the product of SMG evolution (Michalowski et al. 2010). The elliptical galaxies are classified into groups according to their ellipticity. This ellipticity is given by $e = 1 - b/a$, where e is ellipticity, and a and b are the semi-major and semi-minor axes of the galaxy. Higher ellipticity galaxies are on the

left-side of this sequence, denoted as E# where the # sign ranges from 0 to 7 for typically observed elliptical galaxies. In general, ellipticals don't host significant star formation, and therefore appear more red in colour compared to spirals. They may have formed from stellar material created at an earlier stage of their evolution (Sparke & Gallagher 2000). Some literature hypothesizes that $z \sim 0$ elliptical galaxies are the local universe's descendants of sub-millimetre galaxies (Michalowski et al. 2010). In this picture of galaxy evolution, the high stellar masses of SMGs and their substantial contribution to the cosmic star formation rate density at $z \sim 2$ to 3 make them candidates as the progenitors to massive elliptical galaxies (Smail et al. 2004; Michalowski et al. 2010). If this evolution theory is correct, the SMG phase of this evolutionary sequence formed a substantial amount of stellar mass which results in the large populations of long-lived low mass stars we see in the local $z \sim 0$ population. This concept is discussed further is Section 1.3.

1.2.1 SMG morphology

While detailed morphology and kinematics of galaxies requires high spatial resolution observations, existing literature details basic morphology of SMGs. Molecular gas (specifically carbon monoxide) traces the molecular hydrogen in SMGs and is therefore a good option to study their morphologies at high-redshift. Since SMGs are often merging systems, their morphologies vary widely. However, there is a general effective radii of approximately 2 ± 1 kiloparsec (Tacconi et al. 2008; Casey et al. 2014). This effective radii places them approximately twice the size of average local (ultra) luminous infrared galaxies ((U)LIRG)s. SMGs are therefore often called "scaled-up" companions of (U)LIRGs. This effective radii makes

both (U)LIRGs and SMGs significantly smaller than typical spiral galaxies of similar masses (Casey et al. 2014).

Local (U)LIRGs are connected to SMGs in their similar morphologies. Just as SMGs are scaled-up versions of (U)LIRGs in their physical size, they also have significantly higher far-infrared luminosity (Iono et al. 2009). This is apparent in Figure 2.8, where we plot the [N II] 205 μm line luminosity against far-infrared luminosity.

1.2.2 Stellar masses

Sub-millimetre galaxies are extreme objects in many respects. They are known to have extreme high stellar masses. Hainline et al. (2011) used power-law and stellar population synthesis models of optical and mid-infrared fitting in their sample of $\sim$ 70 SMGs to find SMGs have median stellar masses of $\sim 7 \times 10^{10}$ $M_\odot$. These results are on the low-mass end of literature estimates. Most studies, including Michalowski et al. (2010), have determined much higher median stellar masses of $\sim 3.7 \times 10^{11}$ $M_\odot$. Due to the high dust content of SMGs, it is difficult to determine stellar masses since significant corrections must be applied to any optical or ultraviolet SED fit. Therefore there is significant uncertainty on stellar mass measurements in these dusty galaxies. Casey et al. (2014) state uncertainties of a factor of $\sim$ 2 to 3 are typical.

Hayward (2013) used established relationships between sub-millimetre flux density, star formation rate, and dust mass to put an upper limit on the possible stellar masses of SMGs. They predict that at $z \sim 1$, the stellar mass cannot exceed $\sim$ 4 to 7×10^{12} $M_\odot$, while at $z \sim 6$, it cannot exceed $\sim$ 3 to 5×10^{11} $M_\odot$ in typical SMGs.

1.2.3 Star formation rate

SMGs also host some of the most rapid star formation in the universe. Compared to local galaxies and the Milky Way which exhibit ~ 1 $M_\odot$ per year of star formation, SMGs may form hundreds or thousands of solar masses of stars per year. Often, this is determined by observing the far-infrared luminosity since more traditional star formation rate indicators (like the Hα line) are dust obscured. This relationship was presented in Kennicutt (1998):

$$\frac{\mathrm{SFR}}{1\ \mathrm{M_\odot yr^{-1}}} = \frac{\mathrm{L_{FIR}}}{5.8 \times 10^9\ \mathrm{L_\odot}} \tag{1.2}$$

Regardless of whether star formation rate is estimated based on this relationship, or on radiative transfer models (as in Strandet et al. 2017), star formation rates are rapid. Michalowski et al. (2010) find star formation rates in SMGs of ~ 700 $M_\odot$ per year, while Strandet et al. (2017) calculate ~ 4000 $M_\odot$ per year in a likely merging system at $z = 6.9$, depending on the gravitational lensing factor. In a sample of 61 SMGs, Magnelli et al. (2012) find that 26 of these SMGs ($\sim 43\%$) have far-infrared luminosities high enough to support star formation rates ≥ 500 $M_\odot$ per year—if active galactic nuclei (AGN) are not at play in increasing far-infrared luminosity.

1.2.4 Active galactic nuclei and SMGs

Accurately determining star formation rates is simple when applied to samples of SMGs which aren't contaminated by AGN. However, when they are present, AGN may increase far-infrared luminosity by heating dust which artificially inflates star formation rate esti-

mates like that shown in equation 1.2. It is difficult to determine whether an SMG is contaminated by an AGN, but it has been done using various techniques. The presence of AGN can be determined using different tactics including radio emission, near-infrared emission, spectral slope at mid-infrared wavelengths, and optical emission lines (Casey et al. 2014). Unfortunately, the most direct way of determining the presence of an AGN is by observing X-rays. At high-redshift, and in dusty environments, X-rays are difficult to detect since the observations require long observations to collect a sufficient number of X-ray photons. To complicate the picture further, the influence of X-ray binaries is not well understood.

Previous studies have attempted to characterize the fraction of SMGs hosting AGN. Utilizing ultra-deep X-ray observations from the 2 megasecond Chandra Deep Field-North field, Alexander et al. (2005) investigated AGN contamination in their SMGs. They found that up to $\sim 75\%$ of these SMGs were consistent with AGN contamination. Yet other studies have found vastly different results. Casey et al. (2014) provides a good review of these studies, but a typical and recent characterization of AGN contamination was detailed by Wang et al. (2013). They use the Extended Chandra Deep Field-South field to measure that $17^{+16}_{-6}\%$ of their SMGs are AGN contaminated. Across numerous studies, typical findings indicate AGN are present in $\sim 20\%$ of SMGs (Casey et al. 2014), but it is safe to say that this problem is not well understood and is a difficult problem to solve because of the inherent difficulties in observing the effects of AGN at high-redshift in dusty galaxies.

1.3 Motivation for studying SMGs

One of the most important endeavours in modern astronomy is to trace the cosmic star formation rate density ($\rho_{\rm SFR}$) throughout cosmic time. Not only is understanding this inherently important for understanding galaxy evolution, but it sheds light on how quickly galaxies accreted gas from the intergalactic medium, converting gas into stellar mass, and increasing the abundance of heavy elements. To estimate the total star formation rate density of the universe at various redshifts, it is necessary to study it using a wide range of the electromagnetic spectrum. This isn't an easy task, and prior to measurements from the Far-InfraRed Absolute Spectrophotometer (FIRAS) on the Cosmic Background Explorer (COBE) and the Submillimetre Common-User Bolometer Array (SCUBA) on the James Clerk Maxwell Telescope (JCMT) in the 1990s, it was unknown that the universe's energy density at long infrared and millimetre wavelengths is similar to its energy density at the often studied optical and ultraviolet wavelengths (e.g. Dwek et al. 1998; Blain et al. 1999; Casey et al. 2014). This was important because it indicated that a significant amount of star formation, which contributes to the energy density of the universe, must be hidden from optical and ultraviolet observations. In fact, SCUBA observations detected populations of SMGs which were extremely faint ($I \gtrapprox 24$, $K \sim 21$ to 22) at optical wavelengths despite being bright at 850 μm (for example, see Barger et al. 2000).

Furthermore, this hidden star formation is significant, as Wardlow et al. (2011) showed that $\sim 50\%$ of star formation takes place in SMGs at $z \sim 2$. This means that even at "cosmic high-noon" when star formation occured most rapidly in cosmic history, SMGs are

a key component of star formation (Madau & Dickinson 2014).

This discovery emphasized that SMGs are not just extreme objects with a small role in the large-scale structure of the universe, but are connected to the most massive galaxies assembled by $z \sim 2$ (Toft et al. 2014). Toft et al. (2014) details a theoretical evolutionary scheme which put SMGs as progenitors to high stellar mass galaxies including ellipticals at low-redshift. This scheme describes a (likely) merger-driven starburst event in SMGs at high-redshift until the cold gas is consumed (Iono et al. 2009). Often this gas consumption will be due in part to cold gas accretion onto an AGN, which will inevitably quench star formation and leave behind a more compact galaxy with a high stellar mass created during the rapid star formation phase (Toft et al. 2014).

These reasons motivate the important study of SMGs over a wide range of redshifts: their substantial contribution to the stellar mass content of the universe, and their likely role as progenitors to massive elliptical galaxies in the local universe.

1.4 Signatures of sub-millimetre galaxies

Sub-millimetre galaxies have two dominant mechanisms for emitting electromagnetic radiation: dust grain thermal continuum emission; and molecular, and atomic emission lines (Blain et al. 2002). These two components of emission provide a wealth of information about SMGs.

Their dust grain thermal emission is driven by radiative heating of dust from star formation activity, with a long duty cycle estimated to be ~ 0.75 Gyr rather than a short-lived

star-forming event (Narayanan et al. 2015). This means that the sub-millimetre luminous phase in the evolution of SMGs is not a short-lived event. Star-forming processes, including the intensely bright but short-lived O and B type stars, heat dust which then re-radiates the light at longer wavelengths in the far-infrared regime (200 to 1000 μm) (Blain et al. 2002). Dust temperatures in SMGs are typically around 30 to 50 K (e.g. Calanog et al. 2013). These dust temperatures result in a peak wavelength λ_{peak} in the thermal dust emission of approximately 70 to 120 μm (Casey et al. 2014). High dust content is one of the characterizing physical attributes of SMGs, but deriving the dust mass of a given galaxy relies on having photometry of the far-infrared spectrum which thermal dust emission affects (Casey et al. 2014). Typical SMGs have dust masses on the order of 10^8 $M_\odot$ (Casey et al. 2014). Interestingly, the dust-to-gas ratio is consistent with local galaxies: ~ 0.01 (Ivison et al. 2011). The dust emits as a modified blackbody resembling equation 1.1. Modified blackbody equations for this dust come in different forms (see Casey et al. 2014 for details). One simple direct far-infrared modified blackbody model is:

$$S(\nu, T) = \frac{(1 - e^{-\tau(\nu)})\nu^3}{e^{h\nu - kT} - 1} \tag{1.3}$$

In this equation, optical depth τ is given by $\tau(\nu) = (\nu/\nu_0)^\beta$, where $\nu_0 \approx 1.5$ THz, $\beta = 1.5$. Frequency is given by ν, temperature by T, k is the Boltzmann constant, and h is the Planck constant (Casey et al. 2014). In order to estimate the dust temperature of an SMG, far-infrared photometry can be used to constrain the modified blackbody emission curve shown in equation 1.3. In the case of optically thin dust to far-infrared emission, the

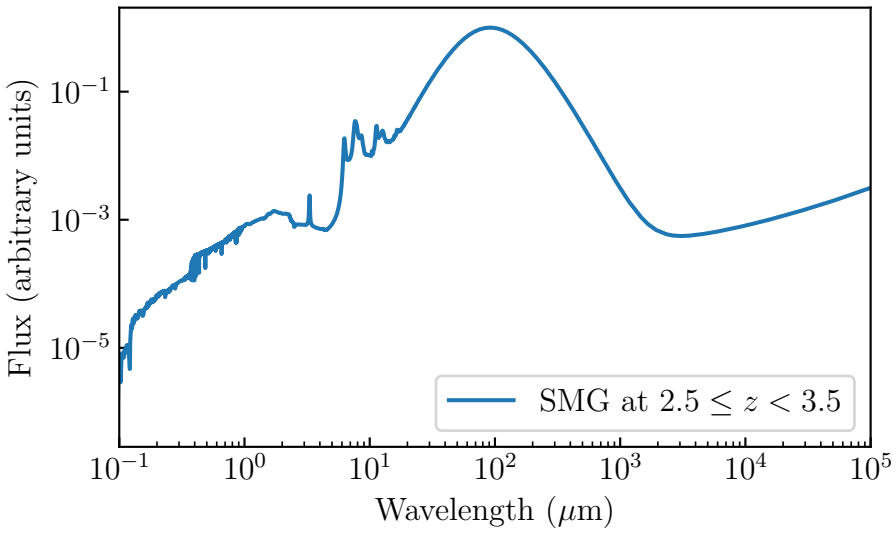

Figure 1.1: An example composite SMG spectrum from the templates provided alongside da Cunha et al. (2015). The redshift is $2.5 \leq z < 3.5$.

$1 - e^{-\tau(\nu)}$ term reduces to ν^{β}.

An example spectrum of an SMG is shown in Figure 1.1. This spectrum is a template from the $2.5 \leq z < 3.5$ binned SMGs originating in da Cunha et al. (2015). It features thermal dust emission, and emission/absorption features.

Emission lines also play an important role in understanding SMGs. Originating from molecular or atomic species, emission lines at far-infrared wavelengths often penetrate through thick dust layers, less attenuated than the traditional optical and infrared emission lines at shorter wavelengths. This long wavelength far-infrared light is often larger than the dust grain size, making the photon and dust grains less likely to interact. When the characteristic size of a dust grain is comparable to the wavelength of incident light, scattering and absorption can cause extinction of that light, converting at least part of the total electromagnetic energy into thermal energy.

One of the most important molecular species emitting spectral lines in SMGs is the carbon monoxide (CO) molecule. Many of carbon monoxide's emission lines are at long enough wavelengths (≥ 500 μm) that they are not effectively obscured by high dust column densities. Furthermore, CO traces molecular hydrogen and therefore molecular gas regions of these galaxies. Its line luminosity can be used to estimate molecular gas mass (Bolatto et al. 2013; Casey et al. 2014):

$$M_{\mathrm{H_2}} = \alpha_{\mathrm{CO}} \times L'_{\mathrm{CO}} \tag{1.4}$$

where L'_{CO} is the CO line luminosity, $M_{\mathrm{H_2}}$ is the molecular hydrogen mass, and α_{CO} is a conversion factor. Various studies determine $\alpha_{\mathrm{CO}} \approx 3$ to 6 $\mathrm{M_\odot}$ $\mathrm{pc^{-2}}$ $(\mathrm{K\ km\ s^{-1}})^{-1}$ as detailed in Casey et al. (2014).

In the South Pole Telescope collaboration, molecular emission from CO was also utilized to determine spectroscopic redshifts for a large number of SMGs (Weiß et al. 2013; Strandet et al. 2016), leading to one of the sample's greatest strengths: knowing its cosmological context.

1.5 The South Pole Telescope sample

1.5.1 Sub-millimetre techniques and observatories

Sub-millimetre astronomy, like astronomy focused at other wavelengths, requires strict weather and atmospheric conditions to be successful. Sub-millimetre light from space is affected by the atmosphere, where water vapour absorption lines make deep cuts in how ef-

fectively certain wavelengths of this light can reach the ground. As a result, sub-millimetre astronomy is typically done by observing specific frequency ranges which allow reasonable atmospheric transmission of sub-millimetre light. For example, the Atacama Large Millimeter/submillimeter Array (ALMA) has a wide frequency range from 500 to 602 GHz (between bands 8 and 9) which no receiver is designed to observe due to the poor atmospheric transmission of the atmosphere to these frequencies.

The best locations for sub-millimetre astronomy are at high altitude, cool, and dry. These three factors reduce the atmospheric absorption and scattering of light. Some of the best locations matching these criteria are Mauna Kea in Hawaii, United States, the South Pole, and the Atacama Plateau in Chile. Mauna Kea hosts JCMT and the Sub-Millimeter Array, while the South Pole hosts the South Pole Telescope (SPT), and the Atacama Plateau hosts ALMA and the Atacama Pathfinder EXperiment telescope (APEX). SCUBA on JCMT played a key role in detecting the earliest populations of sub-millimetre galaxies.

As discussed in Section 1.5.2, achieving high spatial resolution is difficult at long sub-millimetre wavelengths. As a result, some of the most advanced sub-millimetre astronomy uses interferometry observatories such as ALMA. For observations which don't require high spatial resolution, large dishes may be used to observe bright sources or bright emission lines. For example, many of our [C II] 158 μm observations presented in the following sections utilize observations from APEX since this line is very bright and only total flux measurements were sought.

1.5.2 Interferometry

Interferometry is a technique which utilizes the wide-spread spacing of multiple individual telescopes/dishes to artificially increase the effective "diameter" of the primary mirror (in optical astronomy). Assuming a circular aperture, the benefits of increasing the diameter of a primary mirror/dish are easy to demonstrate. The angular resolution, θ, is related to the wavelength of observation, λ, and the primary mirror diameter, D, according to:

$$\theta \propto \frac{\lambda}{D} \tag{1.5}$$

As wavelength increases, the smallest structures which the telescope can resolve increases. As a result, radio and sub-millimetre astronomy requires widely-spread telescope dishes to establish a wide baseline to improve angular resolution: increasing D to decrease θ.

The Atacama Large Millimeter/submillimeter Array utilizes sub-millimetre wavelength interferometry. Depending on the configuration of ALMA, it is capable of using up to 66 dishes comprised of 54 with 12 metre apertures and 12 with 7 metre apertures. The baseline can be adjusted, and can reach up to approximately 16 km. With ALMA, these dishes are transported using specialized vehicles. This means AMLA is able to achieve angular resolutions which other observatories, especially single-dish telescopes, are not able to meet. Furthermore, the addition of multiple dishes means the photon-collecting ability is improved, just as a larger light-collecting surface increases photon capture.

Since our use of ALMA utilizes the Atacama Compact Array (ACA), we do not get the

benefits of better angular resolution which it can provide. However, since our observations require only a total flux measurement, angular resolution isn't required. The large beam-size of ACA will capture all flux from our large angular sources without the need to add flux from resolved components of our gravitationally-lensed objects.

1.5.3 The SPT SMG sample

The South Pole Telescope sub-millimetre galaxy sample (SPT SMG sample) was built using observations from the South Pole Telescope (Carlstrom et al. 2011), and the observations were first presented in Vieira et al. (2010). The South Pole Telescope (SPT) is stationed at the Amundsen-Scott South Pole station in Antarctica, and hosts a millimetre wavelength bolometer camera. The telescope itself is an offset Gregorian (to reduce internal reflection) with a 10 metre aperture. SPT's design is ideal for large scale sky surveys due to its wide field of view of λ(mm units) $\times$ 0.7 deg (Carlstrom et al. 2011). It was designed for cosmological surveys such as investigating galaxy clusters out to $z < 1.5$, and exploring cosmic microwave background anisotropy. However, due to the wavelengths it observes and the redshifted spectral energy distribution of SMGs, it discovered high-redshift populations of these dusty, rapidly star-forming galaxies.

Previous surveys such as Chapman et al. (2003, 2005) found SMGs have a median redshift of approximately "cosmic high-noon" ($z \sim 2$) at $z = 2.2$ with an interquartile range of $z = 1.7 - 2.8$ (Chapman et al. 2005). In comparison, Vieira et al. (2013) found a median redshift of 3.5, but selected these galaxies at 1.4 and 2.0 mm as opposed to Chapman et al. (2003) at 850 μm. Strandet et al. (2016) utilized CO observations to add spectroscopic

redshifts to the Vieira sample of SMGs, measuring a median of $z = 3.9 \pm 0.4$. Vieira et al. (2013) exposed and discovered a bias in the selection of SMGs: longer selection wavelengths more easily detect high-redshift SMGs. This bias is due to the detection wavelength falling on a quickly-varying part of the spectral energy distribution of dusty galaxies. If most dusty galaxies have similar temperatures, than the redshift of the modified blackbody dust emission will be primarily responsible for determining the flux level at a given wavelength. Longer wavelength observations will more easily detect higher redshift sources, since at rest-frame the longer wavelength selection wavelength falls far from the peak of the blackbody emission.

Vieira et al. (2010) presented 87 deg^2 of this field, and detailed the selection criteria and methods used. The survey observed the sky at both 1.4 and 2.0 mm, probing these wavelengths to approximately milliJansky sensitivity, with arcminute resolution.

Using these two wavelengths, it is possible to apply physical reasoning to separate the sample into two classifications. Sources may have a high flux density because they are bright in the far-infrared (from thermal dust emission) or because SPT is observing synchrotron emission. This is accomplished by assuming the emission has the form $S \propto \lambda^{-\alpha}$, where S is the raw flux and α is the 2.0 to 1.4 mm power law index. To classify sources as either synchrotron or thermal dust emission dominated, Vieira et al. (2010) made a cut based on the predicted α value. Dust sources are classified as such if the probability they have $\alpha > 1.66$ is greater than 50%. If this criteria is not met, they are classified as synchrotron emitting sources. This approach leverages the typical SEDs of dusty galaxies—where synchrotron emission and thermal dust emission occur at different wavelengths with op-

posite spectral slopes—to classify sources. When looking at flux levels towards increasing frequency, synchrotron dominated sources should exhibit decreasing flux. Dust emitting dominant sources should show increased flux towards increased frequency, as the observations are "climbing" the spectral energy distribution. Therefore, by comparing the raw flux at these two wavelength observations, an appropriate cut can classify the sources one way or another.

Many sources detected in the SPT SMG survey were determined to be gravitationally lensed. Gravitational lensing is where a distribution of mass located between the observer (in our case, ALMA) and the distant object (our SMGs) bends the path of electromagnetic radiation as a result of a significant gravitational field. The effect is often that the object's measured flux is magnified by this gravitational lens, and therefore to determine its true luminosity, the flux must be de-magnified. De-magnification depends on a gravitational lensing model, such as the lens models presented for SPT SMGs in Spilker et al. (2016) which were derived using 870 μm ALMA imaging. Generally, a luminosity can be de-magnified simply by dividing the raw (gravitationally lensed) luminosity by the magnification factor (μ).

Follow-up observations in Greve et al. (2012) presented Submillimetre Apex BOlometer CAmera (SABOCA) and Large Apex BOlometer CAmera (LABOCA) observations at 350 μm and 870 μm, respectively, allowing the spectral energy distributions of 11 of these submillimetre galaxies to be modelled, constraining their redshifts. In Vieira et al. (2013), 3 mm ALMA observations of 26 of these targets revealed the redshifts of 23 by identifying carbon monoxide lines, and showed 10 of the sources were at $z > 4$.

Since then, the South Pole Telescope Sub-Millimetre Galaxy collaboration has presented more redshifts (see Strandet et al. 2016 for example) and gravitational lensing models (see Spilker et al. 2016) among many other studies investigating the environment and interstellar medium of these sources.

Chapter 2

Studying SMGs using the [C II]-to-[N II] ratio

Fine-structure lines are a key tool in studying sub-millimetre galaxies because these lines penetrate through dust (Draine 2003). For high-redshift galaxies, many of these fine-structure lines are accessible for sub-millimetre observatories like the Atacama Large Millimeter/submillimeter Array (ALMA) in high atmospheric transmittance windows.

Fine-structure lines are useful for studying many galaxies because they can probe various gas properties like density and elemental abundance and their velocity-flux relationships provide information about gas kinematics (Watson & Storey 1980). Two of these fine-structure lines, [C II] with a wavelength of 158 μm, and [N II] with a wavelength of 205 μm in the rest-frame, were the subject of my research project.

2.1 The [N II] 205 μm fine-structure line

The [N II] 205 μm line is a fine-structure emission line which originates from the $^3P_1 \rightarrow {}^3P_0$ transition. The ionization potential of nitrogen is 14.53 eV, similar to hydrogen's 13.6 eV. This means that like ionized hydrogen, ionized nitrogen traces the ionized interstellar medium (Oberst et al. 2006; Zhao et al. 2013; Decarli et al. 2014; Pavesi et al. 2016). An additional feature of [N II] emission is its potential to estimate star-formation rate (Zhao et al. 2013). Its critical density of 44 cm^{-3} at a temperature of 8000 K is fairly low (Oberst et al. 2006). A species' critical density is the condition when the Einstein coefficient of spontaneous de-excitation equals the collisional excitation rate (Casey et al. 2014). As Casey et al. (2014) discuss, it is often assumed that this density must be exceeded for emission of a specific line to take place. [N II] has two important transitions which emit light at wavelengths of $\sim$ 122 μm and $\sim$ 205 μm, each of which have different critical densities. The [N II] 122 μm transition has a critical density much higher than [N II] 205 μm at $\sim$ 290 μm, and as a result the ratio of flux from these transitions is an excellent density diagnostic (Oberst et al. 2006; Herrera-Camus et al. 2016). Langer et al. (2015) shows that the [N II] 205 μm flux increases with electron density approximately linearly until $\sim$ 10 cm^{-3} (Zhao et al. 2016). However, without other fine-structure lines it is not possible to use this line alone to estimate density, as the line luminosity depends on the ionization state of the ISM and nitrogen abundance.

For examples of the [N II] line ratio being used to probe gas density, Herrera-Camus et al. (2016) used this line ratio to investigate densities in nearby galaxies from the *Herschel*

KINGFISH sample, and Goldsmith et al. (2015) used it to estimate gas densities in the Galactic Plane using *Herschel*, finding values typically around $n_{e^-} \sim 10$ to 50 cm^{-3}.

As illustrated in Herrera-Camus et al. (2016), in normal galaxy environments the [N II] 122 μm line is typically brighter than the [N II] 205 μm line, but varies in brightness by a factor of 0.6 to 6. Regardless, each of the [N II] lines are among the brightest lines in actively star-forming galaxies (Brauher et al. 2008).

2.2 The [C II] 158 μm fine-structure line

The [C II] 158 μm line is emitted from the $^2P_{3/2} \rightarrow {}^2P_{1/2}$ transition. Carbon has an ionization potential of 11.3 eV, less than hydrogen's 13.6 eV value. As a result, [C II] emission can originate in neutral and ionized interstellar medium (Stacey et al. 2010; Decarli et al. 2014; Pavesi et al. 2016). It is the most important cooling line in the neutral interstellar medium (Brauher et al. 2008), and is typically optically thin and emitted from regions exposed to the radiation of young stars (Stacey et al. 2010). [C II] 158 μm is also expected to be emitted from photon dominated regions (PDR)s and X-ray dominated regions (XDR)s. PDRs and XDRs are mostly neutral regions of the ISM which still have their chemistry influenced by electromagnetic radiation. The influence (e.g. ionizing specific species) is mainly caused by ultraviolet radiation for PDRs, and X-rays for XDRs. While the gas (mostly hydrogen) may be neutral, it is still possible for carbon to be ionized and emit the [C II] 158 μm line from PDRs. Cooling lines such as [C II] 158 μm cool the interstellar medium by emitting radiation after being collisionally excited. This converts kinetic energy (thermal energy)

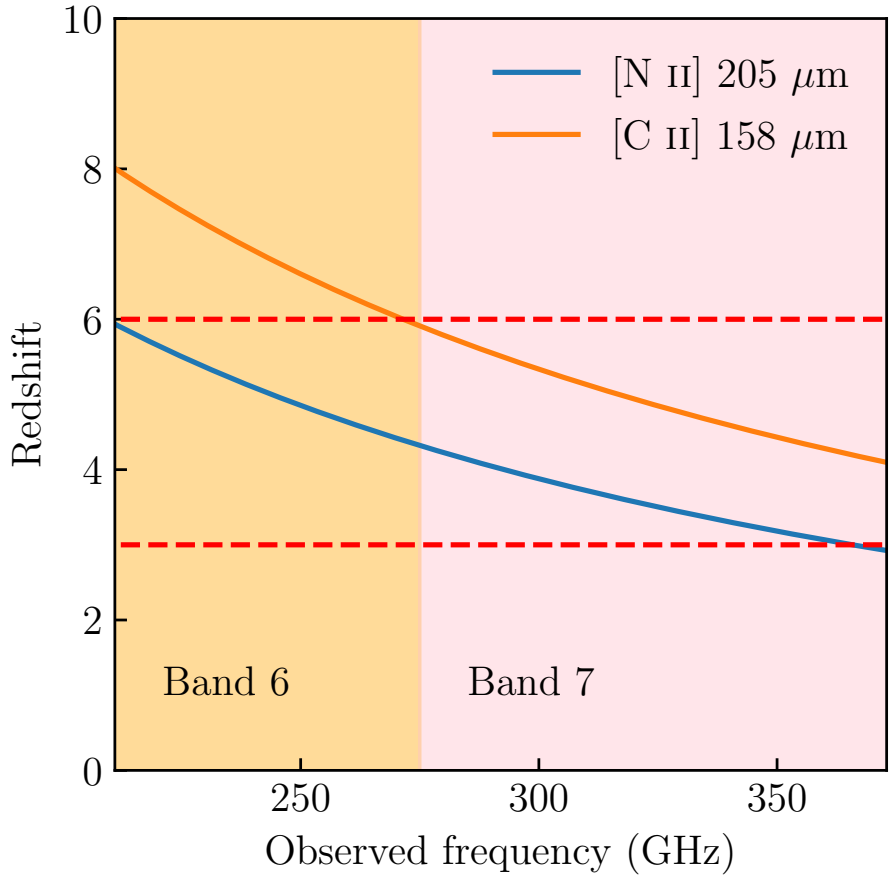

Figure 2.1: A plot of the observed frequencies of [N II] 205 μm and [C II] 158 μm fine-structure lines as a function of redshift. ALMA Bands 6 and 7 are shown as coloured regions, indicating the frequency ranges which they can observe. The red dashed lines show the approximate $3 < z < 6$ range in which ALMA bands 6 and 7 can observe the [N II] 205 μm line.

in the ISM into electromagnetic radiation which (when optically thin to the ISM, or in other words is unobstructed in travelling through the ISM) carries energy away from the galaxy. [C II] 158 μm emission has a high critical density of $n_{e^-} \sim 3000$ cm^{-3} and is among the brightest far-infrared fine-structure lines, significantly brighter than [N II] 205 μm in sub-millimetre galaxies (Brauher et al. 2008, Cunningham et al., in prep.).

Since it is a bright line and importantly traces the neutral and ionized ISM in normal galaxies, it has been detected at high-redshift in many cases (Decarli et al. 2014; Gullberg et al. 2015; Rawle et al. 2014; Riechers et al. 2014; Stacey et al. 2010). Stacey et al. (1991) report that it can account for between 0.1% to 1% of far-infrared luminosity.

Gullberg et al. (2015) reported on [C II] 158 μm detections of approximately 20 gravitationally lensed SPT SMGs between $z = 2$ to 6. For our investigation of the $L_{[C\ II]}/L_{[N\ II]}$ ratio, I first utilized part of the Gullberg et al. (2015) subset of 20 SMGs: the 18 between $z = 3$ to 6. This subset fall into the redshift range where [N II] 205 μm is shifted into ALMA bands 6 and 7 as shown in Figure 2.1. The full published study will include all of our $\sim$ 40 [N II] 205 μm observations, combined with $\sim$ 30 [C II] 158 μm observations to robustly characterize the luminosity ratio at high-redshift.

2.3 Sample selection and data reduction

Before this work, previous research on detected [N II] 205 μm emission from high-redshift ($z > 2$) galaxies have presented either single or few detected lines per study. This is in part due to difficulty in obtaining spectroscopic redshifts for dusty galaxies, and because only for specific redshift windows such as $z =$ 3to 6 is the [N II] 205 μm easily accessible from the ground (as it falls into high atmospheric transmittance windows). For examples, see Béthermin et al. (2016); Decarli et al. (2014); Nagao et al. (2012); Pavesi et al. (2016); Umehata et al. (2017). For the first time, this research presents a large, uniformly selected sample of high-redshift ($z > 2$) [N II] 205 μm detections that characterizes the $L_{[C\ II]}/L_{[N\ II]}$

distribution in high-redshift dusty galaxies including sub-millimetre galaxies. This entire sample of SMGs are gravitationally lensed (with lensing models provided in Spilker et al. 2016), allowing us to observe faint [N II] 205 μm lines which would otherwise require longer integrations. Gravitational lensing increases our observed luminosities, and affects the image we observe directly as the original view of the galaxy is bent around a gravitational potential. The lens may even cause different surface brightness features. Depending on the lensing geometry, Einstein rings (a ring-shaped image) may be generated. However, our study does not rely on spatially resolving any source and instead only total flux measurements are obtained.

Our data was collected during ALMA Cycle 4, with project code 2016.1.00133.T (PI: Chapman). We targeted sources with redshifts in the range $z = 3$ to 6. At these redshifts, the [N II] 205 μm line falls into ALMA ACA bands 6 and 7 (see Figure 2.1). These sources are a subset of the sources with [C II] 158 μm observations in Gullberg et al. (2015), only excluding two sources which had redshifts of $z < 3$ (outside of band 6 and 7 coverage). Furthermore, this redshift range is less susceptible to the reduced atmospheric transmittance seen in higher frequency ALMA bands. The Atacama Compact Array (ACA) of the ALMA observed our sources.

Principal Investigator Chapman chose to use ACA for these observations because the total flux measurement of the [N II] 205 μm line does not require high-resolution, and therefore does not require a large baseline for the observing antennae. While the smaller 7 metre dishes used with ACA are less sensitive than the 12 metre dishes used in other ALMA configurations, it is sufficient to detect our bright, gravitationally-lensed sources with reasonable

$\sim 3\ \sigma$ line detections (see Figure 2.4). Combined with the lower overhead times for ACA observations, its large beam size ($\sim$ 6") makes it the ideal choice for these measurements, especially when considering the large median Einstein radii of 0.64 arcseconds seen in the SPT SMG sample (Spilker et al. 2016).

We reduced the [N II] data using the Common Astronomy Software Applications package CASA version 4.7 (McMullin et al. 2007). The standard ALMA pipeline product images typically exhibited over-subtraction of the continuum, leading to wide, deeply negative flux wings at velocities outside of the typical $\sim$ 500 km s^{-1} line full-width at half-max. To fix this, we used CASA's CLEAN function to iteratively deconvolve the interferometric data and generate new model images. This involves converting flux in the "dirty" image into perfect point sources in the "model" image.

We performed no *uv*-continuum subtraction, since we typically found that within $\sim$ 2000 km s^{-1} of the zero-point velocity our baseline flux was constant within noise, and the continuum subtraction tended to over-subtract the [N II] line. As a result, we were consistently able to reliably subtract a constant baseline level to isolate the line. For consistency, images were generated with a resolution of 150 $\times$ 150 pixels and approximately a 1.0" pixel size. Beam sizes were typically around 5 to 7" along the semi-major axis, much larger than the median Einstein radii of 0.64 arcseconds (Spilker et al. 2016). This large beam size is due to the compact configuration of ACA, reducing angular resolution compared to more extended ALMA configurations. However, the larger beam size makes total flux measurements easier since the entire source is contained within one beam and not spread into different components. Our [N II] observations are not resolved even for our largest sources, a point which

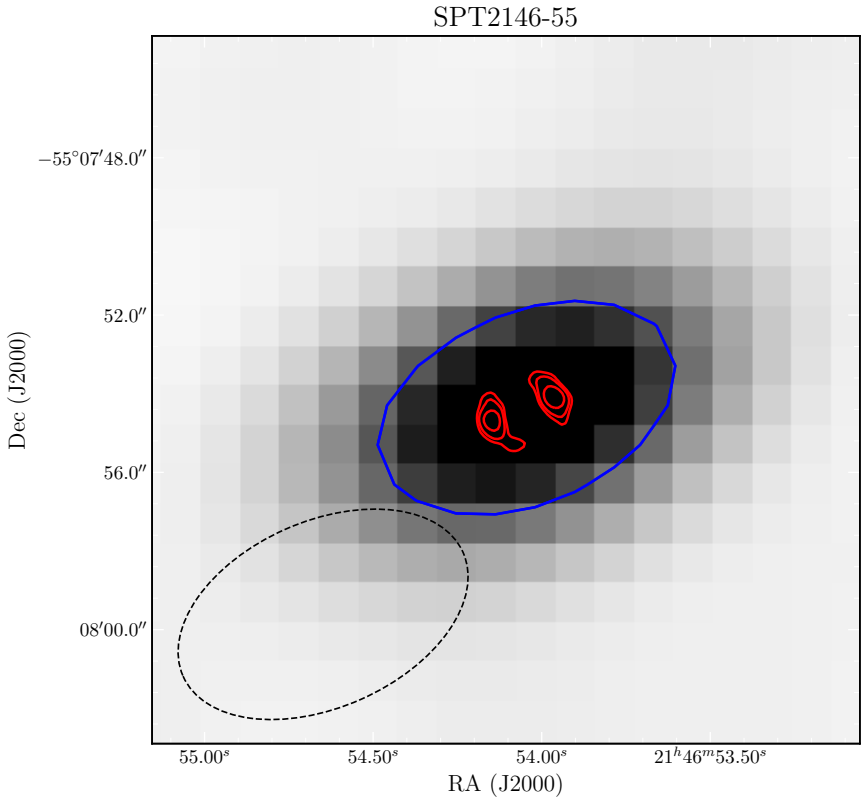

Figure 2.2: An example of our ACA [N II] line observations. Here we show SPT2146–55, a galaxy we observed in ACA band 6, as a channel map. The red contours represent continuum from higher resolution ALMA imaging, and demonstrate that the ACA beam does not resolve even the largest lensed SMGs in our sample. The blue contour represents the full-width at half-max (FWHM) of the [N II] ACA observations. The beam size is represented in the bottom left corner by the black dashed line ellipse.

is illustrated by Figure 2.2 and Figure 2.3. SPT0418–47 and SPT2146–55 are among the sources with the largest angular sizes in our sample, each of which are unresolved in our ACA Band 6 and 7 images. In these figures, the red contours represent high-resolution ALMA imaging, revealing a ring shaped image of SPT0418–47 and a pair of flux sources in the case of SPT2146–55.

To obtain velocity-flux line profiles, we extracted flux from the peak flux pixel in our

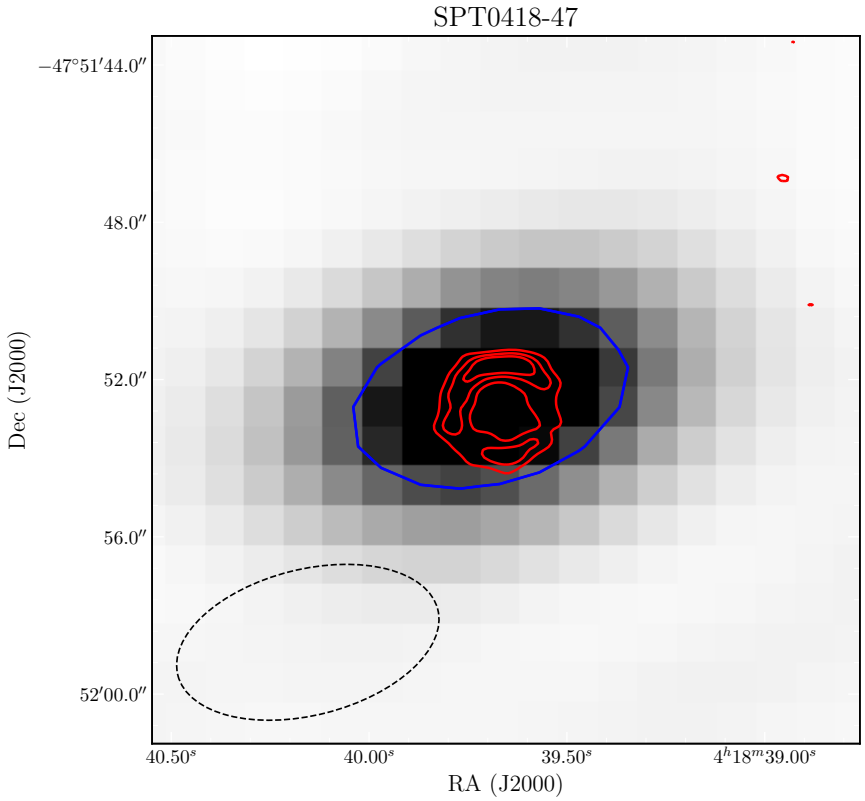

Figure 2.3: An example of our ACA [N II] line observations. Here we show SPT0418–47, a galaxy we observed in ACA band 7, as a channel map. The red contours represent continuum from higher resolution ALMA imaging, and demonstrate that the ACA beam does not resolve even the largest lensed SMGs in our sample. The blue contour represents the FWHM of the [N II] ACA observations. The beam size is represented in the bottom left corner by the black dashed line ellipse.

[N II] spectral cubes (normally the central pixel). To ensure that this extracted all flux, we also extracted flux from an elliptical aperture region of comparable size to the beam, around 1× to 1.5× the semi-major axis size. This method had a negligible effect on the total flux measurement, importantly not increasing the total integrated value. These line profiles are shown in Figure 2.4.

To determine the total line flux, we take this extracted line profile and subtract a constant

flux (representing the baseline) to bring the flux to zero (within noise) in the off-line regions. At this step, we have only significant positive flux at the location of the fine-structure line. Next, we utilize the high signal-to-noise CO molecular line observations of these sources in our analysis (see for example Weiß et al. 2013). We fit these CO spectra with a single-peak Gaussian curve, and determine its full-width at half-max (FWHM). Then we summed the

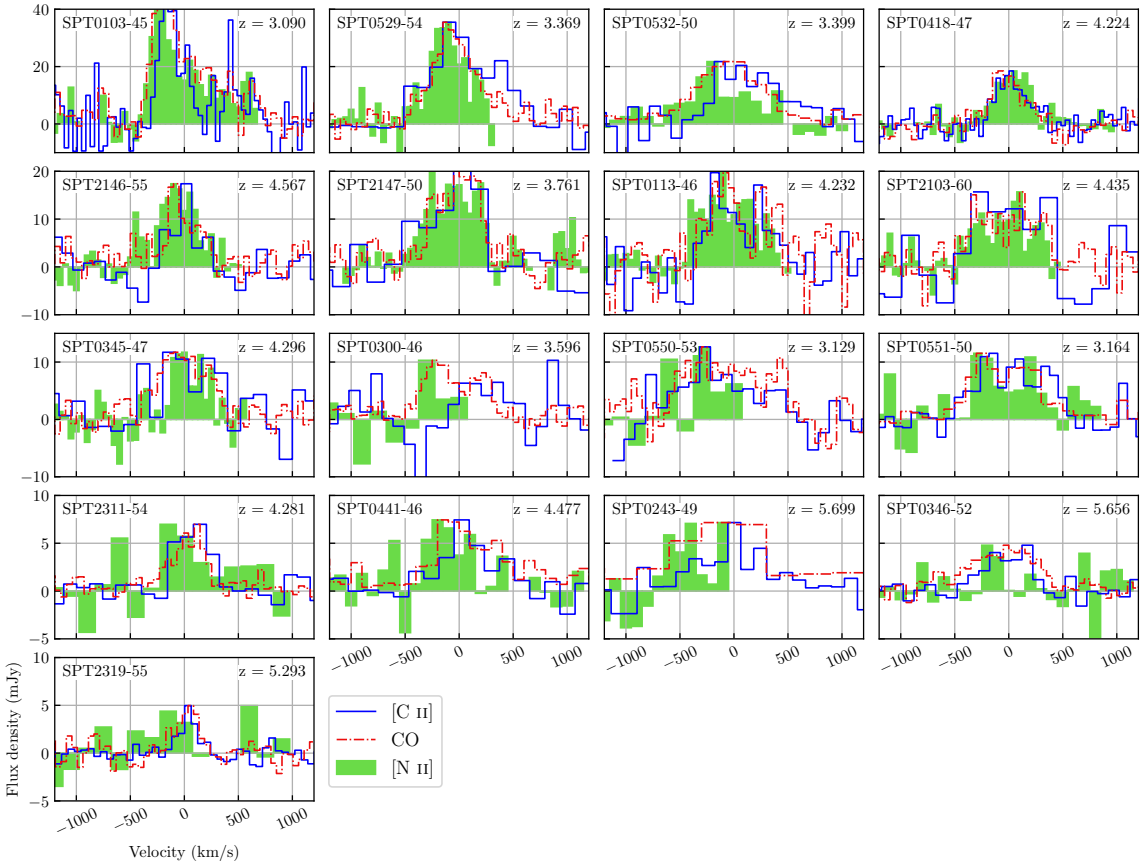

Figure 2.4: Velocity-flux line profiles for 17 SPT SMGs. This plot includes [N II] 205 μm as green histograms, [C II] 158 μm as a blue solid line, and CO line profiles as a dash-dotted red line. From top to bottom, the vertical axis decreases going down the rows. The [C II] and CO fluxes are normalized to the peak flux in the [N II] observation. The velocities are zeroed according to redshifts from Strandet et al. (2016). Redshifts are indicated in the top-right corner of each panel.

[N II] 205 μm and [C II] 158 μm (data from Gullberg et al. 2015, but reimaged) flux over a range of two times the CO line FWHM value ($2\times$ FWHM$_{\rm CO}$) to be consistent in determining the total [N II] and [C II] flux. If we assume that the [N II] and [C II] emission have a similar widths as the CO line, then this method should be accurate and more reliable than fitting the [N II] or [C II] line profile with a Gaussian. Indeed, in our highest signal-to-noise [N II] detections (see Figure 2.4, top row) we see a high level of agreement in the shapes of the line profiles. In many sources shown in Figure 2.4, we see that the weak emission would be difficult to capture with a Gaussian fit. When attempting Gaussian fits, many sources required fine-tuning of the "first guess" fit parameters for the code to succeed.

In a few cases (SPT0300–46, SPT0550–53, and SPT0243–49), the entire [N II] 205 μm line was not covered by our ACA observations. In these cases, to reduce project overhead the spectral coverage was not complete to keep total project time below 50 hours. For these sources, the [C II] and [N II] flux is summed within the $2\times$ FWHM$_{\rm CO}$ range which has spectral coverage in all three lines, meaning we only sum flux at velocities where both [C II] and [N II] has been covered with observations.

2.4 Results

Of the 17 new [N II] 205 μm observations presented in Cunningham et al. (in prep.), we detect 11 with $> 4.5\sigma$, with 3 sources detected at $\geq 3\sigma$. Combining these measurements with Béthermin et al. (2016), we have built a sample of 15 high-redshift [N II] 205 μm detections, the largest uniformly selected sample put together to date. In our remaining 3

undetected [N II] 205 μm lines, we put an upper limit calculated as 3$\times$ the root-mean-square of the off-line flux (Cunningham et al. in prep.). We use gravitational lensing models from Spilker et al. (2016) to de-magnify our line luminosities by dividing by the gravitational lensing factor, μ.

We detect lensed [N II] 205 μm luminosities varying between approximately 1 to 15 mJy km s^{-1}, and measure lensed [C II] 158 μm luminosities between 18 to 170 mJy km^{-1} (see Table 2.1).

2.4.1 $L_{[C\ II]}/L_{[N\ II]}$ versus L_{FIR}

We observe the $L_{[C\ II]}/L_{[N\ II]}$ ratio in our SPT SMG sample, finding an interquartile range of approximately 12, between 10.7 to 22.6. We find a median value of $L_{[C\ II]}/L_{[N\ II]}$ 12.9 ± 4.5. Figure 2.6 shows the distribution of $L_{[C\ II]}/L_{[N\ II]}$ in our SMG sample in the form of a histogram, while Figure 2.5 shows $L_{[C\ II]}/L_{[N\ II]}$ as a function of far-infrared luminosity.

These values are consistent with the majority of the literature, particularly consistent with local (U)LIRGs which exhibit a median ratio of $\sim$ 9, and span a similar range in $L_{[C\ II]}/L_{[N\ II]}$. However, our SPT SMGs show statistically higher $L_{[C\ II]}/L_{[N\ II]}$ values. Our high-redshift literature sources have a median $L_{[C\ II]}/L_{[N\ II]} \sim 19$, higher than our SPT SMG sample but captured within the range of values we observe in SMGs. With so few high-redshift literature sources published, this could be the result of small number statistics. Overall, the ratios we observe are consistent with the literature, as our extreme $L_{[C\ II]}/L_{[N\ II]}$ sources are among the highest and lowest published (e.g. Pavesi et al. 2016; Umehata et al. 2017). Based on modelling performed by Oberst et al. (2006); Nagao et al. (2012); De-

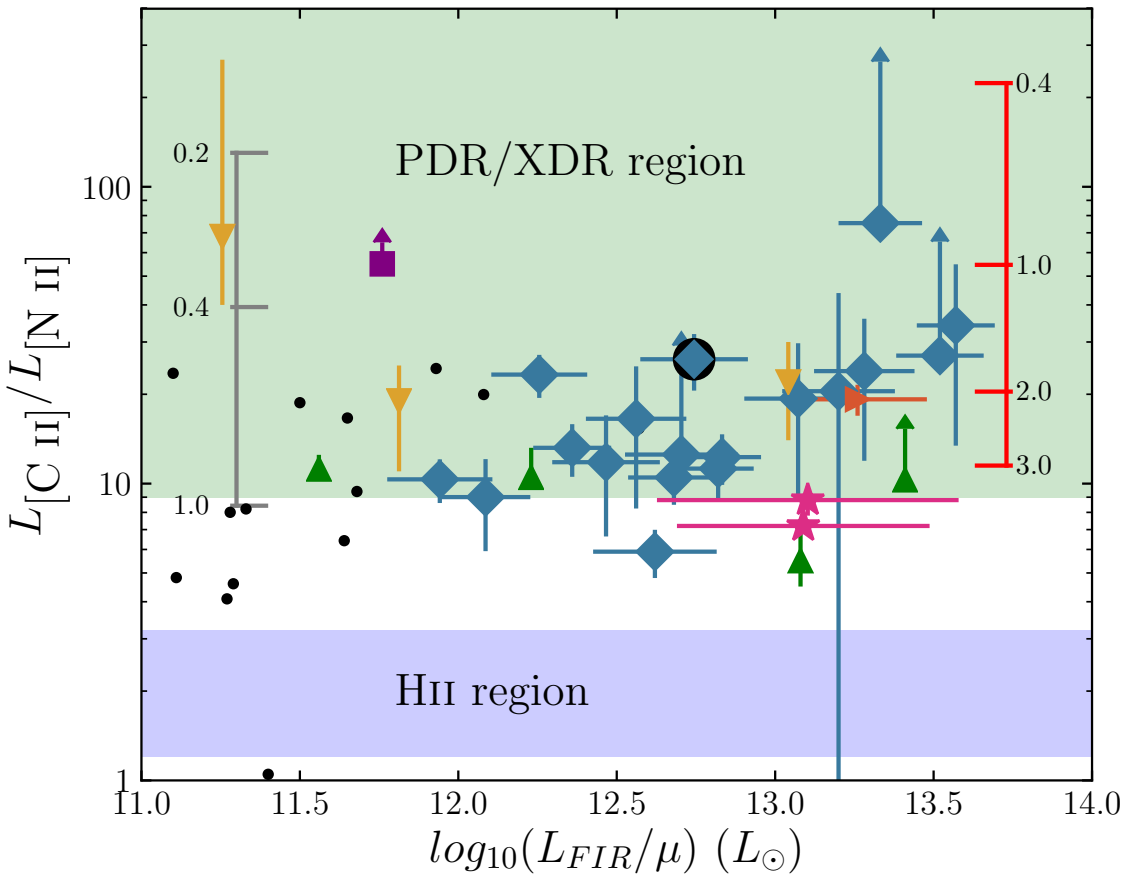

Figure 2.5: A plot of $L_{[C\ II]}/L_{[N\ II]}$ versus far-infrared luminosity for our SPT SMGs and a number of literature sources. Ratio regimes expected for H II regions and PDR/XDR zones are shown using a coloured background (based on Decarli et al. 2014). Metallicity grids for ionization parameter $\log(U_{H\ II}) = -3.5$ and ISM densities $\log(n) = 1.5$ (grey) and 3.0 (red) are shown (Nagao et al. 2012). These grids have units of $Z/Z_\odot$. The source SPT2132–58 has a black circular background. The upwards green triangles represent $z \sim 4.7$ sources from Decarli et al. (2014), which include two Lyman alpha emitters, a SMG, and a QSO in order of increasing far-infrared luminosity. Downward yellow triangles represent $z \sim 5.3$ to 5.7 sources from Pavesi et al. (2016), including a Lyman-break galaxies, a far-infrared luminous LBG, and a massive SMG in order of increasing far-infrared luminosity. The purple square represents a $z = 3.1$ Lyman alpha blob from Umehata et al. (2017). The rightward orange triangle represents an SMG at $z = 5.243$ from Rawle et al. (2014). Two components of an unlensed protocluster of SMGs, SPT2052–56, are shown as pink stars (Pass et al. in prep.). Local LIRGs are shown as black dots. They are assembled from Lu et al. (2017); Díaz-Santos et al. (2017); Zhao et al. (2016).

carli et al. (2014) the high values we find indicate that the [C II] 158 μm emission in the SPT SMGs is dominated by photon dominated regions and X-ray dominated regions. If [C II] 158 μm emission was dominantly emitted from ionized gas regions where [N II] 205 μm emission also originates, we would expect much lower $L_{[C\ II]}/L_{[N\ II]}$ values, and the emission would be particularly susceptible to the relative abundance of ionized carbon and nitrogen. While future studies will reduce the unknowns such as gas density and ionization parameter, these results are consistent with existing literature that the [C II] 158 μm emission is dominantly emitted from PDR/XDR regions in high-redshift dusty galaxies.

There is no obvious trend of $L_{[C\ II]}/L_{[N\ II]}$ increasing or decreasing as a function of L_{FIR}, although there is a subtle increase in ratios for sources with $L_{FIR} > 10^{13}$ $L_{\odot}$. This tells us there is no systematic effect of increasing $L_{[C\ II]}/L_{[N\ II]}$ as a function of far-infrared luminosity, which would directly probe the effect of active star formation on the abundance of ionized carbon and nitrogen, and the fractional abundance of ionized and neutral gas. Our future paper examining the entire $\sim$ 40 SPT SMGs might shed more light on if this ratio has a robust relationship with L_{FIR}.

2.4.2 $L_{[C\ II]}/L_{[N\ II]}$ versus T_{dust}

We also investigate the relationship of the $L_{[C\ II]}/L_{[N\ II]}$ as a function of dust temperature. This relationship is shown in Figure 2.7. In Gullberg et al. (2015), it was reported that the far-infrared luminosity normalized [C II] 158 μm emission decreased towards higher dust temperatures. This was attributed to less efficient gas heating in galaxies with a strongly far-ultraviolet ionizing field (Malhotra et al. 1997; Gullberg et al. 2015). However, when

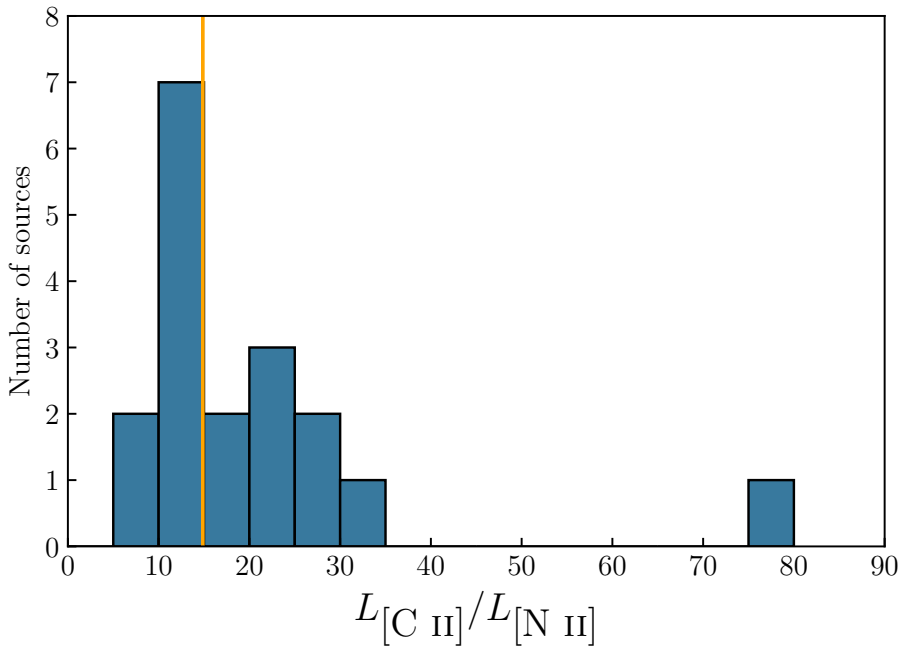

Figure 2.6: A histogram of our observed $L_{[C\ II]}/L_{[N\ II]}$ values in our South Pole Telescope Sub-millimetre Galaxies. The vertical solid orange line represents the median ratio value for the SPT SMGs.

testing our sample for this, the scatter in ratios prevents us from capturing this possible trend.

Similarly to our results of de-magnified $L_{[N\ II]}$ versus dust temperature, we see no clear trend of dust temperature on the [N II]-to-[C II] luminosity ratio. There is a significant amount of scatter in our measurements, but overall we see a clustering of our SPT SMGs and high-redshift literature sources at dust temperatures $\sim$ 35 to 45 K. The full sample of $\sim$ 30 SMGs with $L_{[C\ II]}/L_{[N\ II]}$ may help resolve any existing relationship.

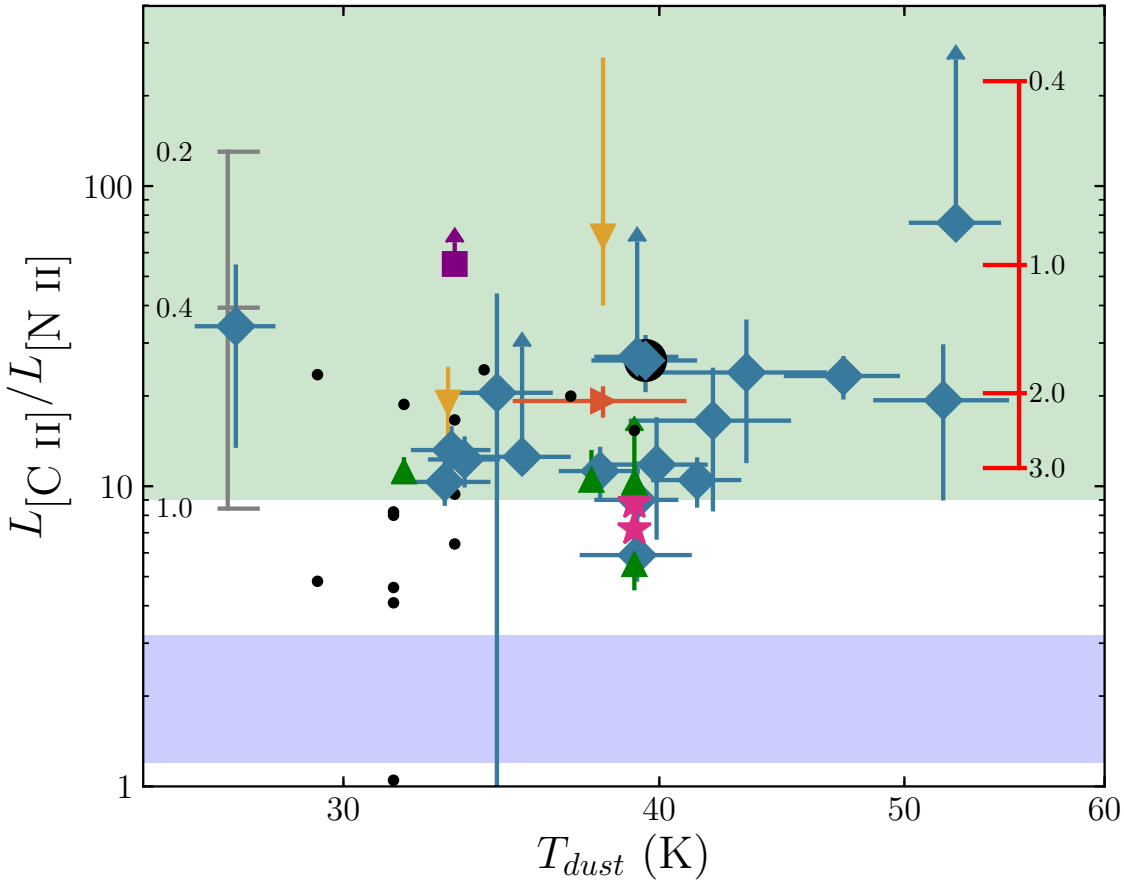

Figure 2.7: A plot of $L_{[C\ II]}/L_{[N\ II]}$ versus dust temperature for our SPT SMGs and literature sources. Ratio regimes expected for H II regions and PDR/XDR zones are shown using a coloured background (based on Decarli et al. 2014). Metallicity grids for ionization parameter $\log(U_{H\ II}) = -3.5$ and ISM densities $\log(n) = 1.5$ (grey) and 3.0 (red) are shown (Nagao et al. 2012). For explanation of what objects and references the literature sources originate from, see the caption of Figure 2.5.

2.4.3 De-magnified $L_{[N\ II]}$ versus L_{FIR}

Investigating the relationship between de-magnified $L_{[N\ II]}$ luminosity against de-magnified far-infrared luminosity sheds light on the radiative thermal emission from dust (resulting in the extreme far-IR luminosities typical of SMGs) and the ionization conditions of the galaxy's ISM. In the absence of AGN, the dust and ionized gas regions will both be directly

influenced by the radiation coming from young, hot stars. While dust will absorb the radiation and re-emit it at longer wavelengths, nitrogen may be ionized when photons carry sufficient energy. As a result, we expect to see increasing $L_{[N\ II]}$ with increasing L_{FIR}. This relationship is shown in Figure 2.8.

We observe that the de-magnified [N II] 205 μm luminosity increases with small (~ 0.3 dex) dispersion towards increasing demagnified L_{FIR}. We fit this relationship according to the equation:

$$\log_{10}(L_{[N\ II]}) = \alpha \times \log_{10}(L_{FIR}) + b \tag{2.1}$$

Fitting the de-magnified $L_{[N\ II]}$ versus de-magnified L_{FIR} relationship in our SMG sample, we observe a slope of $\alpha_{SMG} = 0.49 \pm 0.17$ and $b = 2.2 \pm 2.2$. This slope is unitless because both the demagnified $L_{[N\ II]}$ and L_{FIR} values have units of solar luminosities ($L_\odot$). We plot all sources including lower limits as though they hold true values. As a result, it is likely our measured slope is slightly lower than the true value, but given the small dispersion we see in this relationship it is unlikely the lower limits are far from their true values.

We choose not to fit all literature sources since both our SMG sample well represents the distribution of various literature sources in this relationship, but also because of the significant sample bias differences between different literature sources. Instead, we fit local (U)LIRGs, the sample assembled from Lu et al. (2017), Díaz-Santos et al. (2017), and Zhao et al. (2016). We calculate a slope of $\alpha_{(U)LIRGs} = 0.27 \pm 0.23$ and $b = 4.3 \pm 2.7$. This means we measure a shallower slope in local (U)LIRGs compared to our SPT SMG sample.

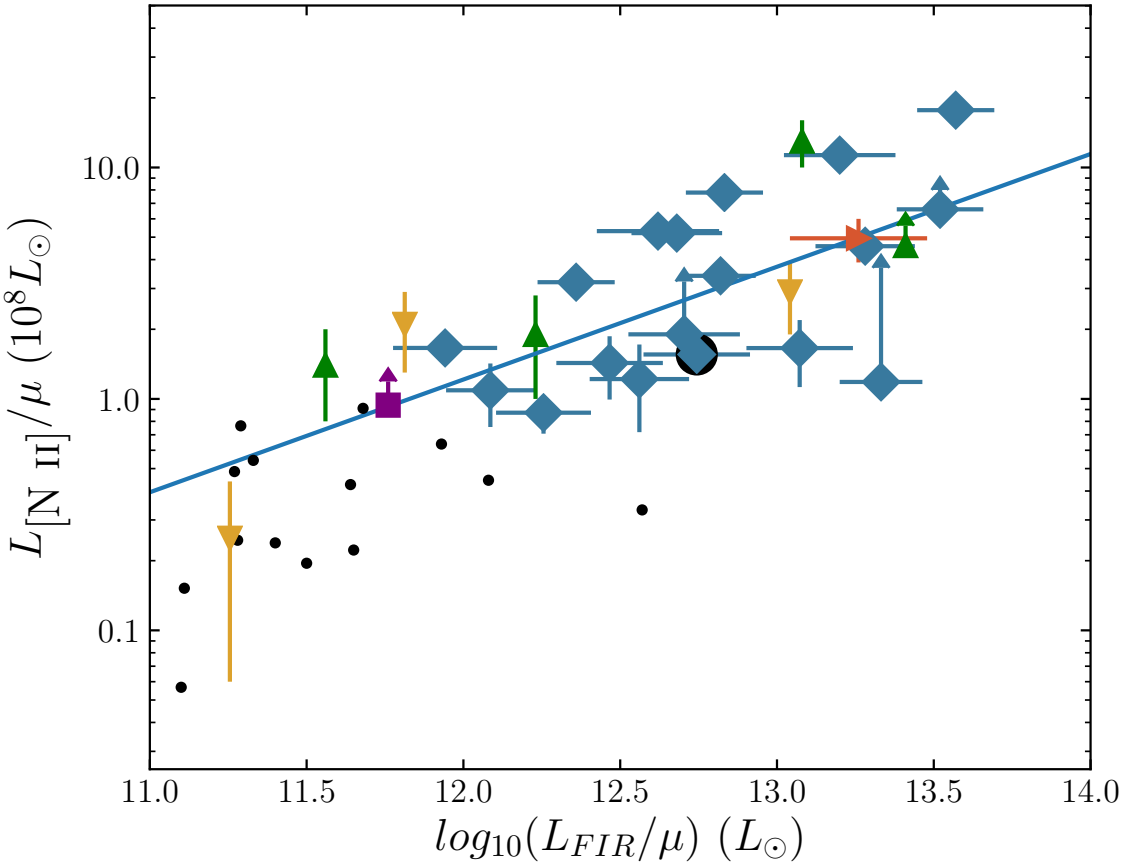

Figure 2.8: A plot of demagnified [N II] 205 μm luminosity versus far-infrared luminosity in our SPT SMGs and literature sources. Refer to the caption of Figure 2.5 for details and references of the literature sources. The solid blue line represents a linear regression fit to the SPT SMGs alone.

2.4.4 De-magnified $L_{[N\ II]}$ versus T_{dust}

We also investigate the de-magnified $L_{[N\ II]}$ luminosity against dust temperatures. This is plotted in Figure 2.9. This relationship is affected by efficiency of gas heating by young, hot stars (Malhotra et al. 1997; Gullberg et al. 2015). In cases where the ultraviolet and optical radiation efficiently heats dust, we would expect the $L_{[N\ II]}$ value to increase towards higher dust temperatures. If dust heating is inefficient or varies significantly between galaxies, we

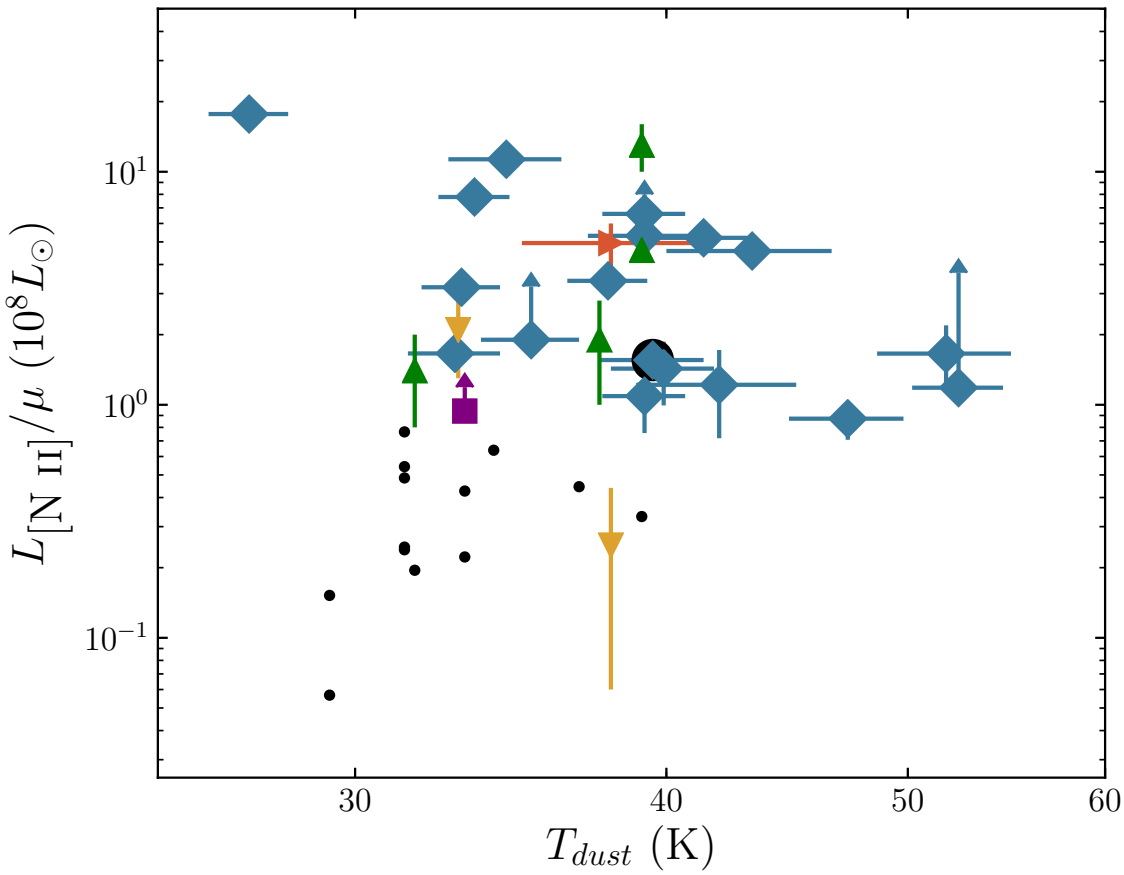

Figure 2.9: A plot of demagnified [N II] 205 μm luminosity versus dust temperature in our SPT SMGs and literature sources. Refer to the caption of Figure 2.5 for details and references about the literature sources.

would not expect to see a defined relationship.

We fail to observe any clear relationship between de-magnified $L_{[N\ II]}$ and dust temperature, T_{dust}. This relationship is shown in Figure 2.9. While our sub-millimetre galaxy sample extends over a wider range of dust temperatures than local (U)LIRGs and our literature sample, we fail to capture any trend. There is significant scatter in our [N II] 205 μm luminosities, especially in the highly occupied temperatures between $32 < T_{dust} < 45$ K.

Likewise, while our literature sources span a narrower interquartile range of temperatures than our SPT SMGs, it's clear there is no consistent relationship between $L_{[N\ II]}/\mu$ and T_{dust}.

2.5 Discussion and analysis

This selection of high-redshift [N II] 205 μm detections represents the largest uniformly selected sample to date. By utilizing our combination of [N II] 205 μm and [C II] 158 μm detections, we are able to provide the first robust characterization of the luminosity ratio of the [C II] and [N II] lines at high-redshift. Furthermore, our detections cover a wide range in far-infrared luminosity, spanning between approximately $L_{FIR}/\mu = 10^{12}$ to $10^{13.7}$ $L_{\odot}$. Prior to our measurements, this range of far-infrared luminosity was sparsely sampled in robust $L_{[C\ II]}/L_{[N\ II]}$ detections, with few literature studies (see caption of Figure 2.5 for examples).

We measure a median value of $L_{[C\ II]}/L_{[N\ II]}$ 12.9$\pm$4.5, with an interquartile range of $\sim$ 12, spanning between $L_{[C\ II]}/L_{[N\ II]} \sim$ 10.7 to 22.6. These results are consistent with $L_{[C\ II]}/L_{[N\ II]}$ values presented in existing literature, such as Decarli et al. (2014), Umehata et al. (2017), Pavesi et al. (2016), and Rawle et al. (2014). These high $L_{[C\ II]}/L_{[N\ II]}$ imply [C II] 158 μm emission dominated in neutral gas including PDRs and XDRs, as lower ratios would indicate emission of [C II] 158 μm and [N II] 205 μm from the same gas clouds. Our observed values of $L_{[C\ II]}/L_{[N\ II]}$ extend throughout the highest ratios observed in Umehata et al. (2017) and Pavesi et al. (2016), and through the lowest observed Decarli et al. (2014) and Pass et al. (in prep.), indicating a wide range of physical conditions (fractional abundance of ionized and neutral ISM) in our SMGs. We also find values of $L_{[C\ II]}/L_{[N\ II]}$ approximately equal

to and greater than the previous record holder for sub-millimetre galaxies, SPT2132–58 presented in Béthermin et al. (2016). Furthermore, they are similar to values found in local (U)LIRGs (Lu et al. 2017; Zhao et al. 2016; Díaz-Santos et al. 2017), but are systematically at higher values. (U)LIRGs assembled from these studies exhibit an median of approximately $L_{[C\ II]}/L_{[N\ II]} \sim 8.8$, with a mean of ~ 11.8 and an interquartile range of ~ 13, spanning between ~ 5.2 to 18.2. This indicates that we are likely observing [C II] 158 μm emission which is more dominated by emission from neutral PDR/XDR regions compared to local (U)LIRGs, where [C II] 158 μm emission from ionized region plays a more active role.

2.5.1 Existing models of $L_{[C\ II]}/L_{[N\ II]}$

The systematic difference in $L_{[C\ II]}/L_{[N\ II]}$ values in local (U)LIRGs and our high-redshift sub-millimetre galaxies could be the result of many different physical differences. Physical parameters like metallicity, gas density, the ionization parameter, and the fractional abundance of neutral versus ionized interstellar medium all play a role in affecting the emission of [N II] 205 μm and [C II] 158 μm. To investigate the parameter space which affects this ratio, we consider some models presented in Oberst et al. (2006), Nagao et al. (2012), and Pavesi et al. (2016).

Oberst et al. (2006) model the expected [C II]/[N II] line ratio for an ionized gas region. They assume that because the critical densities of electron excitation for these two lines are similar, their flux ratio will primarily depend on the abundances of ionized carbon and nitrogen. Oberst et al. (2006) assume a density of $n(C^+)/n_{e^-} = 1.4\times10^{-4}$ for ionized carbon and $n(N^+)/n_{e^-} = 7.9 \times 10^{-5}$ for ionized nitrogen. Their model predicts a [C II]/[N II] flux

ratio of ~ 3 at low gas densities ($< 10^1$ cm^{-3}) and ~ 4.3 at high gas densities ($> 10^3$ cm^{-3}), with a dip to [C II]/[N II] < 3 around 20 to 100 cm^{-3}. This modelling demonstrates that gas density can have a significant effect ($\sim 30\%$) on the flux and luminosity ratios of the [N II] 205 μm and [C II] 158 μm lines.

Nagao et al. (2012) presented observations of a $L_{[C\ II]}/L_{[N\ II]}$ measurement for a sub-millimetre galaxy at $z = 4.76$ along with modelling using CLOUDY (Ferland et al. 1998). In their model, Nagao et al. (2012) assume a pressure-equilibium gas cloud. The gas cloud is described by specifying gas density and ionization parameter (at the illuminated surface). They employ four combinations of these parameters with $\log(n_{H\ II})= 1.5$ and 3.0, and ionization parameter $\log(U_{H\ II})= -3.5$ and -2.5. With each model, they varied metallicity ($Z_{gas}/Z_{\odot}$) between 0.05 and 3.0. At the extremes, Nagao et al. (2012) predict small [C II]/[N II] ratios at low gas densities but high ionization parameter and metal rich gas, and low (< 1) [C II]/[N II] ratios in metal-poor, high density, low ionization parameter environments. The effect they predict is substantial, with the flux ratio spanning almost three orders of magnitude even for the same gas density and ionization parameter models, varying only metallicity. In these models the gas density has a significant effect, increasing the [C II]/[N II] ratio in all cases with fixed ionization parameter and metallicity. Decreasing the ionization parameter has the same, but less extreme effect.

Pavesi et al. (2016) also perform CLOUDY modelling (Ferland et al. 2013). Their results are similar to Oberst et al. (2006), showing that increasing gas density increases the expected $L_{[C\ II]}/L_{[N\ II]}$ value. Their models align with Nagao et al. (2012) in that gas density is a more effective parameter in varying the line ratio compared to the ionization parameter. Unique

to these models, though, Pavesi et al. (2016) vary starburst age, doing models with an age of 1 Myear and 10 Myear. The age of the starburst affects the highest mass stars still emitting light, and therefore affects the radiation field hardness (Pavesi et al. 2016). Their models show that at low ionization parameters, regardless of gas density, older starbursts result in higher $L_{[C\ II]}/L_{[N\ II]}$ values. Conversely, at high ionization parameters, regardless of gas density, older starbursts result in lower $L_{[C\ II]}/L_{[N\ II]}$ values, whereas for log(U)= -3.0 to -2.0, the effect is entangled with the effects of gas density. Harder radiation fields should result in more production of doubly-ionized nitrogen, N^{++}, causing less emission of [N II] lines from N^{+} ions.

2.6 Future Plans

Studying the $L_{[C\ II]}/L_{[N\ II]}$ distribution at high-redshift is valuable because it provides insight into physical properties of the interstellar medium of these galaxies by utilizing some of the brightest lines they emit. It can be sensitive to the fractional abundance of ionized and neutral interstellar medium, the gas metallicity, gas density, and even the ionization parameter. However, it has limitations which are primarily the result of the wealth of physical parameters in the ISM which may affect its value. The gas density, the ionization parameter, the hardness of the radiation field from star formation, or the fractional abundance of ionized and neutral gas in these galaxies all have consequences which affect this ratio. As a result, breaking the degeneracy of this parameter space is important in truly gaining an understanding of what the $L_{[C\ II]}/L_{[N\ II]}$ luminosity ratio means.

Table 2.1: Observed properties for our 18 SMGs presented in Cunningham et al. (in prep.). Redshifts are provided from Strandet et al. (2016), while lensing models and μ values can be found in Spilker et al. (2016).

Source	z	$S_{[\mathrm{N\ II}]}$ (Jy km s^{-1})	$\mu L_{[\mathrm{N\ II}]}$ (10^{10} L$_\odot$)	$S_{[\mathrm{C\ II}]}$ (Jy km s^{-1})	$\mu L_{[\mathrm{C\ II}]}$ (10^{10} L$_\odot$)
SPT0103-45	3.090	15.43 ± 2.93	0.4 ± 0.08	145.41 ± 6.46	4.88 ± 0.22
SPT0529-54	3.369	14.2 ± 2.8	0.42 ± 0.08	144.13 ± 5.95	5.57 ± 0.23
SPT0532-50	3.399	11.33 ± 2.26	0.34 ± 0.07	97.55 ± 1.76	3.82 ± 0.07
SPT0418-47	4.224	6.74 ± 1.05	0.29 ± 0.04	119.97 ± 2.44	6.64 ± 0.13
SPT2146-55	4.567	7.29 ± 1.24	0.35 ± 0.06	33.12 ± 2.79	2.07 ± 0.17
SPT2147-50	3.761	9.7 ± 1.84	0.34 ± 0.07	78.21 ± 3.49	3.61 ± 0.16
SPT0113-46	4.232	9.31 ± 1.5	0.4 ± 0.06	73.86 ± 3.38	4.1 ± 0.19
SPT2103-60	4.435	6.65 ± 2.17	0.31 ± 0.1	45.74 ± 3.56	2.73 ± 0.21
SPT0345-47	4.296	3.04 ± 1.57	0.13 ± 0.07	44.57 ± 2.55	2.53 ± 0.14
SPT0300-46[a,b]	3.596	1.60 ± 0.60	5.30 ± 2.0	-3.80 ± 2.3	-0.16 ± 0.1
SPT0550-53[b]	3.129	4.27 ± 4.9	0.11 ± 0.13	67.72 ± 4.36	2.32 ± 0.15
SPT0551-50	3.164	6.58 ± 4.0	0.18 ± 0.11	173.06 ± 4.09	6.03 ± 0.14
SPT2311-54	4.281	1.98 ± 1.0	0.09 ± 0.04	36.77 ± 1.31	2.08 ± 0.07
SPT0441-46	4.477	3.95 ± 1.74	0.18 ± 0.08	35.38 ± 1.53	2.14 ± 0.09
SPT0243-49[a,b]	5.699	1.9 ± 2.48	0.13 ± 0.17	18.26 ± 3.44	1.59 ± 0.3
SPT0346-52[a]	5.656	0.98 ± 2.53	0.06 ± 0.17	58.03 ± 1.46	5.0 ± 0.13
SPT2319-55	5.293	1.38 ± 0.69	0.08 ± 0.04	17.77 ± 0.7	1.39 ± 0.05

[a] Considered a lower-limit $L_{[\mathrm{C\ II}]}/L_{[\mathrm{N\ II}]}$. [N II] 205 μm detection not significant enough to consider robust. [b] The [N II] spectra for these sources does not have sufficient baseline to completely cover the CO line profiles. The fluxes quoted are summed at velocities where but [N II] and [C II] spectra are present.
SPT2132-58 values found in Béthermin et al. (2016).

To break this degeneracy and to gain valuable information about the gas density in the ISM, the South Pole Telescope Sub-Millimeter Galaxy collaboration submitted an ALMA-ACA Cycle 6 proposal to observe the [N II] 122 μm line in a subset of our sources with [N II] 205 μm measurements (Principal Investigator Cunningham). The proposal also included requests to observe the [N II] 205 μm line in sources excluded from the Cycle 4 [N II] 205 μm proposal. These goals are now within reach due to increased availability of ALMA band 8, providing access to the $\sim$ 375 to 500 GHz frequency domain. The proposal was accepted and should be observed during ALMA Cycle 6.

These observations will provide detections of the [N II] 122 μm line for 14 SPT SMG sources using ALMA bands 7 and 8. The [N II] 122 μm line falls into ALMA band 8 for approximately $3.9 < z < 5.4$, and into band 7 for $5.6 < z < 7.95$. Therefore, to line up our possible [N II] 122 μm observations, we select our [N II] 205 μm observed sources within $3.9 < z < 6$. Furthermore, we requested observations of the [N II] 205 μm in sources at lower redshift ($2 < z < 3$) than our existing sample, which could expand the redshift range of our [N II] 205 μm detections to $2 < z < 6$, and therefore expand our $L_{[C\ II]}/L_{[N\ II]}$ throughout a wider redshift range.

Herrera-Camus et al. (2016) and Zhao et al. (2016) showed that the ratio of [N II] 122 μm to [N II] 205 μm flux is effective in determining gas densities. The two lines have different critical densities of 44 cm^{-3} for the 205 μm transition and 290 cm^{-3} for the 122 μm transition at a temperature of 8000 K (Herrera-Camus et al. 2016). Zhao et al. (2016) determined gas densities using this ratio in 12 (U)LIRGs, finding they range from around 1 to 100 cm^{-3}, with a median of 22 cm^{-3}, while Herrera-Camus et al. (2016) found ranges from 1 to 300

cm^{-3} with a median of $\sim$ 30 cm^{-3} in spatially resolved extragalactic regions. As shown in Langer et al. (2015), the [N II] 122 to 205 μm line ratio increases above $n_{e^-} \sim 10$ cm^{-3} from approximately 0.6 to 6.0 around 300 cm^{-3} (Herrera-Camus et al. 2016).

This proposal hopes to achieve measurements of the total flux ratio of the [N II] 122 and 205 μm transitions to constrain gas density in these sources, and to help break the degeneracy of physical ISM parameters causing variation in the $L_{[C\ II]}/L_{[N\ II]}$ distribution.

Chapter 3

A narrow-band survey of high-redshift star formation

A critical component to understanding the evolution of the universe is how the cosmic star formation rate has changed over cosmic time. Researchers may study the star formation rate at different redshifts by observing starlight from young, short-lived O and B type stars, by inferring it from the modified blackbody emission from dust (the re-processed ultraviolet radiation from young stars) where there is little effect from AGN heating, or by observing nebular emission lines arising in the ionized gas surrounding the young, hot stars associated with star formation rate and gas properties. We have embarked on a survey with the Canada-France-Hawaii Telescope that aims to utilize the narrow-band selection technique to identify emission lines in galaxies associated with star formation. The survey was designed to be substantially deeper than previous wide-field surveys, while still covering

a ~ 2 deg^2 region to be representative and relatively free of cosmic variance. By observing the emission of specific lines from galaxies at different redshifts, it is possible to infer on average how much star formation is occuring in a volume of the universe (star formation rate density). Previous research such as Lilly et al. (1996) has shown that the cosmic peak of star formation occured at $z > 1$, with more recent literature indicating around $z \sim 2$ (Madau & Dickinson 2014). Here, I describe a new narrow-band emission line survey undertaken by international collaborators Scott Chapman, Tracy Webb, Sara Ellison, Marcin Sawicki, Suresh Sivanandam, Bob Abraham, John Blakeslee, Arif Babul, Johan Richard, Thierry Contini, Roser Pello, Laurence Tresse, and Roland Bacon called the Wide-field High-redshift Extragalactic Emission Line survey (WHEELS).

3.1 Narrow-band Survey introduction and motivation

Tracing the star formation rate density ($\rho_{\rm SFR}$) from large galaxy surveys is challenging, in part because the selection wavelength can lead to different results. There are significant observational biases which cause disagreement between surveys at different wavelengths. For instance, ultraviolet light is easily attenuated by dust and therefore star formation in dusty galaxies is more difficult or impossible for these ultraviolet surveys to detect (Cucciati et al. 2012; Geach et al. 2008). The ultraviolet survey presented in Cucciati et al. (2012) measured the star formation rate density of $\log_{10}(\rho_{\rm SFR}) = -0.62^{+0.49}_{-0.09}$ M$_\odot$ yr^{-1} Mpc^{-3} for the $z = 1.7$ to 2.5 range. Geach et al. (2008) with a much longer central survey wavelength of 2121 nm measured $\log_{10}(\rho_{\rm SFR}) = -0.77^{+0.29}_{-0.33}$. Surveys at longer wavelengths also have

disadvantages. For instance, surveys which use infrared wavelengths still struggle to detect lower luminosity galaxies in the distant universe, limited to $\gtrapprox 10^{11} L_{\odot}$ at $z > 2$ even with typical ALMA observations. Infrared surveys may also lose accuracy because of difficulties in detecting less luminous sources, and therefore require estimates for ρ_{SFR} contribution from dim sources (Geach et al. 2008).

To solve this intrinsically difficult problem, narrow-band emission line surveys offer a complementary approach to identifying distant star forming galaxies. Narrow-band emission line surveys such as the High-redshift Emission Line Survey (HiZELS) (see Geach et al. 2008; Best et al. 2013, and Sobral et al. 2015 for details) and studies such as Drake et al. (2015) utilize wide-field narrow-band observations in combination with broad-band imagery to detect line emitting galaxies. These surveys look for sources which appear brighter in the narrow-band filter compared to the broad-band filter. With careful selection criteria which account for photometric uncertainty, these surveys can build large samples of line emitting galaxies at various redshifts.

3.1.1 Survey description

Our narrow-band survey utilizes the WIRCam wide-field infrared camera aboard the Canada-France-Hawaii Telescope to observe extragalactic survey fields with existing broad-band imagery. The intent is to use narrow-band imaging over a large area of the sky to detect specific emission lines at different redshifts. The end goal is to produce 3×3 mosaics (roughly 1 deg^2, with WIRCam's $\sim$ 20' field of view) in various fields to reach a total sky area of approximately 2.2 deg^2. By observing a wide region of the sky with a narrow wavelength

range and comparing the image to an image of a wider wavelength range (at roughly the same central wavelength), we can determine with reasonable certainty which galaxies are emitting strong lines.

We target the Hα λ6563, [O III] λ5007, [O III] λ4959, Hβ λ4861, and [O II] λ3727 emission lines. These lines will hit the 2320 nm central wavelength of WIRCam's CO filter at redshifts of $z \sim 2.53$, 3.63, 3.68, 3.77, and 5.22, respectively. This means we are probing the star formation at three distinct epochs in cosmic time at $z \sim 2.5$, $z \sim 3.7$ and $z \sim 5.2$. This is illustrated in Figure 3.1.

The first stages of this survey involve observations with CFHT WIRCam, of approximately 30 or 15 hours per telescope pointing to generate deep 2320 nm images. Next, detecting emission in our narrow-band images and matching our detections to sources in existing K-band imagery. By comparing calculated magnitudes in these two images, we can determine which sources show a narrow-band excess (brighter magnitude in narrow-band filter compared to broad-band filter). Then utilizing photometric redshift catalogues to determine which galaxies are the best candidates for follow-up observation with spectroscopy.

3.2 Introduction to CFHT and WIRCam

The Canada-France-Hawaii Telescope (CFHT) is an optical and infrared telescope with a primary mirror 3.6 m in diameter. It is approximately 4 km above sea level in Hawaii, USA. One of the key instruments which CFHT uses to observe the sky is the Wide-field InfraRed Camera (WIRCam). WIRCam is a near infrared mosaic camera mounted on CFHT, capable

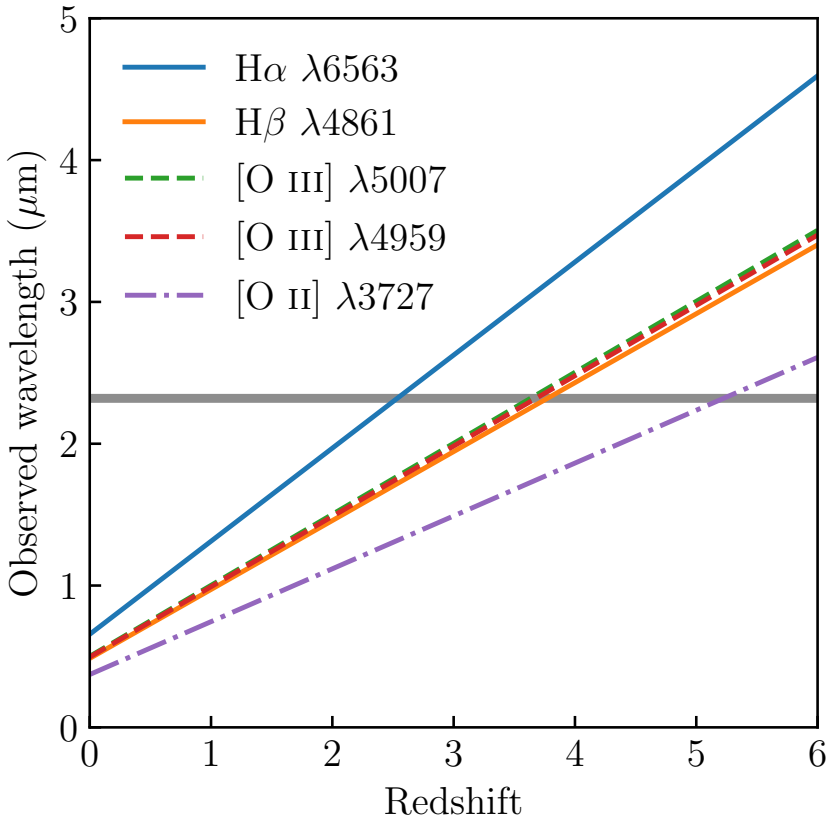

Figure 3.1: An illustration of the observed wavelength of the emission lines versus redshift in our narrow-band emission line survey. The horizontal grey region represents the CO filter onboard WIRCam, with a bandwidth of 40 nm and a central wavelength of 2320 nm. The lines will be observed at three key redshift ranges, $z \sim 2.5$, $z \sim 3.7$ and $z \sim 5.2$.

of wide-field imaging of wavelengths of approximately 1000 to 2300 nm. It has four detectors, each with resolution of 2048×2048 pixels, which are arranged in a 2×2 configuration. This results in a field of view of approximately 20'×20' (Puget et al. 2004). This places its pixel scale at $\sim 20'/(2048\text{pix} \times 2) \sim 0.3'$ pix^{-1}.

WIRCam has many filter options available, with central wavelengths ranging between 1020 to 2320 nm. For our survey, we utilize the CO filter, which is the longest wavelength narrow-band filter available for WIRCam at 2320 nm, with a bandwidth of 40 nm.

3.3 Methods and observational setup

To identify galaxies with a narrow-band excess in emission (an observed brighter magnitude in the narrow-band compared to broad-band), we must compare the WIRCam observations directly to existing broad-band imagery. For our observations in the UDS field, we utilized K-band imagery which is publicly available. This imagery was produced using the United Kingdom Infrared Telescope (UKIRT) during the UKIRT Infrared Deep Sky Survey (UKIDSS) (see Lawrence et al. 2007; Casali et al. 2007 for details). The Ultra-Deep Survey (UDS) field is a subset of the UKIDSS survey that covers approximately 0.8 deg^2 and contains extremely deep J, H, and K band imagery. The Data Release 3 imagery in UDS has a limiting K band AB magnitude of m = 23.7 (5σ depth). Furthermore, the UDS field has photometric redshifts for many galaxies, which James Simpson matched to our narrow-band excess sources to determine candidates for follow-up spectroscopic observations (see Cirasuolo et al. 2007 for details). We also observed portions of the Cosmic Evolution Survey (COSMOS) field since it (and UDS) have sufficiently deep images at in the K-band to not limit our narrow-band survey and a wealth of complementary data at many wavelengths. A cutout of an early UDS field observation is shown in Figure 3.2.

When taking the difference in magnitudes calculated from the narrow-band and broad-band images, $\mathrm{K}-\mathrm{CO}$, potential emission line emitting galaxies will have a difference greater than zero: $\mathrm{K}-\mathrm{CO} > 0$. High-redshift galaxies should have $m_{\mathrm{K}} \approx m_{\mathrm{CO}}$ (Bunker et al. 1995). However, small differences in magnitudes could be due to variation in how the images are reduced, photometric errors, or atmospheric conditions. Therefore, we apply a confidence

level "cut" to estimate the significance of emission excess. We follow the approach of Bunker et al. (1995), Geach et al. (2008), and Sobral et al. (2015) by applying a criteria in selecting the confidence in our narrow-band excess galaxies:

$$m_{\rm K} - m_{\rm CO} = -2.5\log(1 - \Sigma\delta 10^{-0.4(c-m_{\rm CO})}) \tag{3.1}$$

where δ, representing the photometric error is defined as:

$$\delta = \sqrt{\pi r_{\rm ap}^2(\sigma_{\rm CO}^2 - \sigma_{\rm K}^2)} \tag{3.2}$$

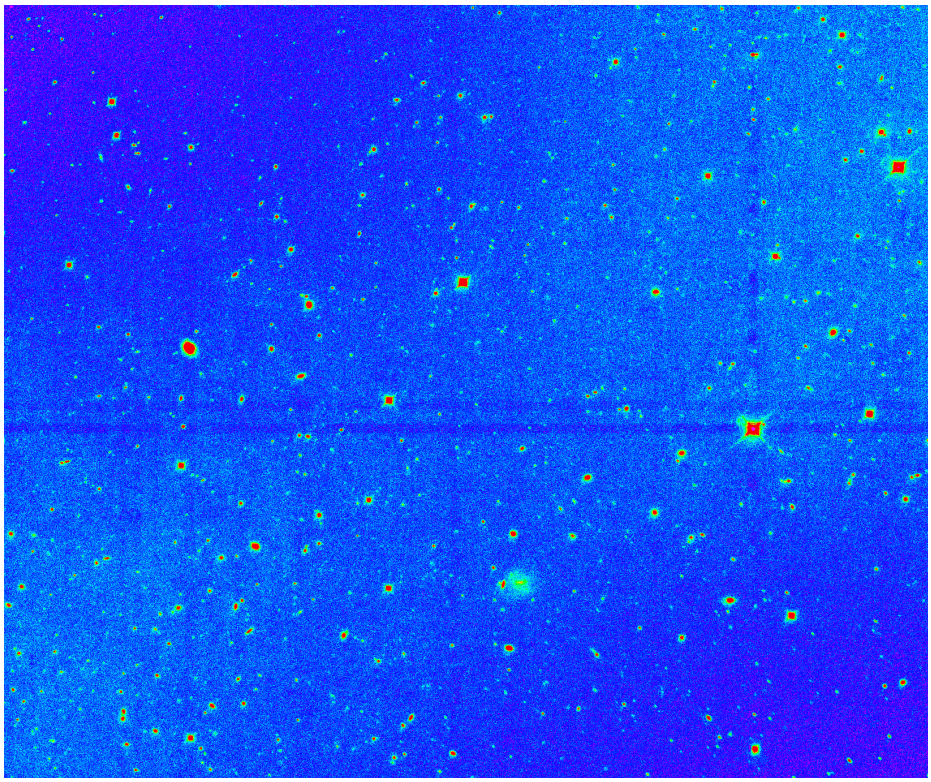

Figure 3.2: A reduced image from chip-2 of WIRCam. This is a pointing in the UDS field.

In equation 3.1, c represents the zero-point of the narrow-band image while Σ represents the "significance cut number", which is similar to the standard signal to noise level (Bunker et al. 1995). $\sigma_{\rm CO}$ and $\sigma_{\rm K}$ represent photometric uncertainties, and $r_{\rm ap}$ is the aperture radius (Bunker et al. 1995). Geach et al. (2008) and Sobral et al. (2015), assume Σ values of 2.5 and 3, respectively.

All Canada-France-Hawaii Telescope observations were performed with the same method. We use the CO filter with a central wavelength of 2320 nm and a bandwidth of 40 nm. We request K-band seeing conditions of 0.65 to 0.8" and an airmass of < 1.2. We use the DP16 dithering pattern with one exposure per dither pattern position, with 200 second micro-exposures, repeated until the entire observation time is used. This is intended to help reduce the effect of the thermal background on our infrared wavelength observations.

3.4 Current status

Currently, we have two 100% complete CFHT WIRCam programs targetting two fields (UDS and COSMOS) for 45 hours each. These observations have resulted in a 1×2 configuration of our intended 3×3 mosaic in each field. For each field, the 45 hours are divided into two pointings: a central 30 hour integration and an offset 15 hour integration. The offset integration is targetted to be near the edge of the field of view from the central pointing. A more recent program in semester 18A has not been completed due to restrictions on time available for the right ascension we requested.

Initial results indicate that we detect narrow-band excess approximately a magnitude

fainter (see Figure 3.3) than the results presented in Geach et al. (2008). This implies that even while extending to higher redshifts than the HiZELS survey, we can effectively build a large sample of galaxies to build the luminosity functions of the various emission lines we are detecting. We present a histogram detailing the photometric redshift matches for an initial stacked image in the UDS field in Figure 3.4.

Recently released observations in a DEEP2 survey field were observed in CFHT WIRCam

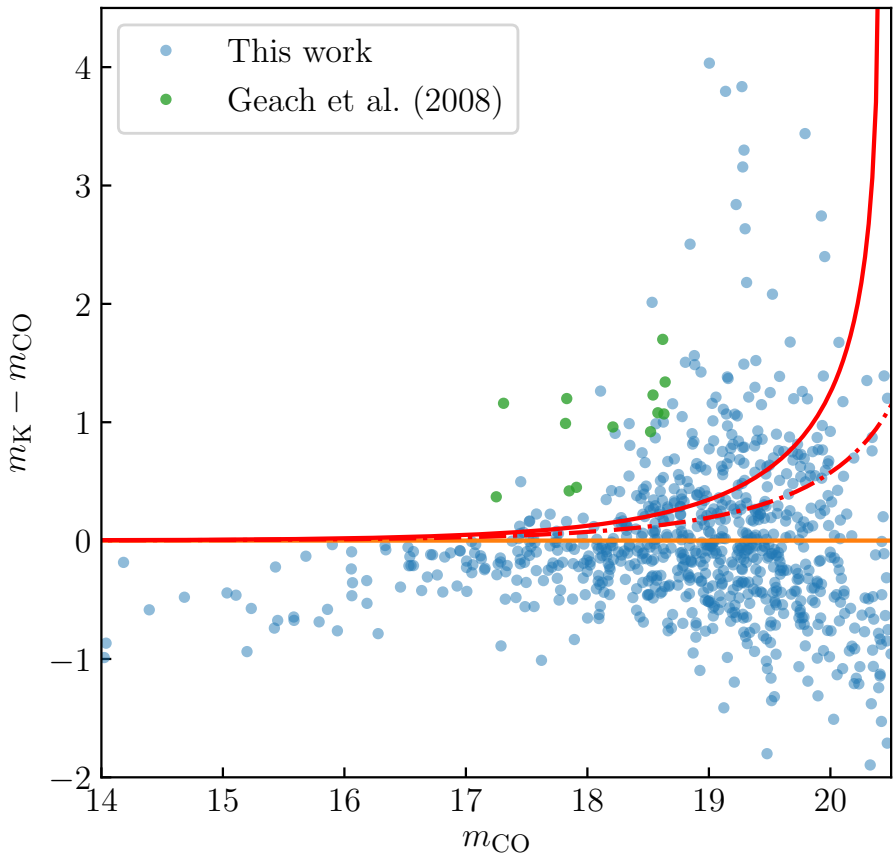

Figure 3.3: An initial plot of the difference in broad-band minus narrow-band magnitudes from out survey, including two significance cuts. The solid red line indicates a significance cut of $\Sigma = 5$, while the dash-dotted red line represents $\Sigma = 3$. Refer to equation 3.1 for details.

Table 3.1: Details of the WHEELS survey completed to date. For each field, the 45 hours of integration time is divided into a 30 hour and a 15 hour pointing. The 30 hour pointings are centered on the field center, while the 15 hour pointings are located alongside this center in Right Ascension, but the same declination.

Field name	RA, Dec hh:mm:ss.ss, ±dd:mm:ss.s	Semester	Integration hours	Completeness
UDS	02:17:30.00, -05:12:00.0	16B	45	100%
COSMOS	10:10:29.80, +02:15:01.6	17A	45	100%
DEEP2	23:30:00.00, +00:00:00.0	18A	3.7	18.6%

semester 18AC33 (see Table 3.1).

Following methods described in the previous section, we generated a list of sources to observe with follow-up spectroscopy. A successful Gemini Near-InfraRed Spectrometer (GNIRS) program (Principal Investigator Cunningham, Program ID GN-2017B-Q-62) observed approximately 15 of our narrow-band excess candidates. The next steps in this project are to reduce this GNIRS data to determine if the observed objects are emitting the expected emission lines.

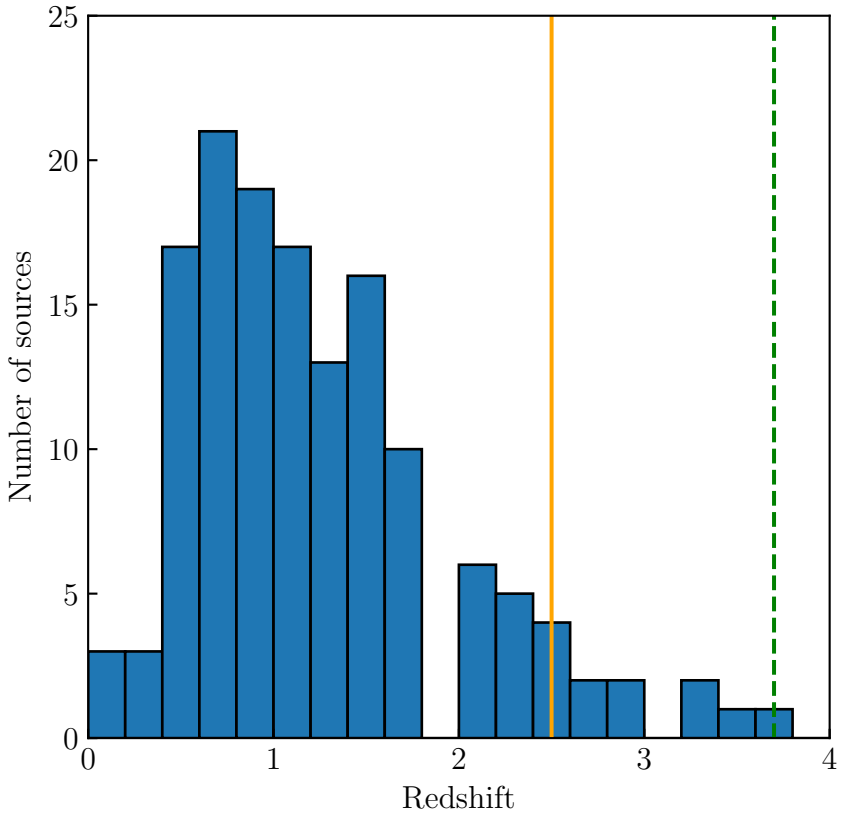

Figure 3.4: A histogram showing the results of an initial match of narrow-band excess objects to a photometric redshift catalog. The orange vertical dashed line indicates the redshift at which we expect to detect Hα λ6563 emitting galaxies. The green solid vertical line indicates the redshift at which we expect to detect Hβ λ4861 or [O III] emitting galaxies. No detected narrow-band excess sources matched with photometric redshifts at higher redshifts than shown here.

Chapter 4

Conclusion

4.1 Studying SMGs using the [C II] -to-[N II] ratio

Utilizing ACA observations of the [N II] 205 μm line in high-redshift sub-millimetre galaxies, we have characterized the distribution of the $L_{[C\ II]}/L_{[N\ II]}$ for the first time. Our new observations targeted approximately 40 SMGs with $z = 3$ to 6, and here we analyzed the first 18 which had accessible [C II] 158 μm data presented in Gullberg et al. (2015). Existing literature which has measured the [N II] line in high-redshift galaxies has only reported on detections of at most a few sources (see Decarli et al. 2014; Pavesi et al. 2016; Umehata et al. 2017 for examples), making our sample the first large, uniformly selected collection of high-redshift [N II] 205 μm measurements. Furthermore, these measurements probe a wide range of demagnified far-infrared luminosity of $\sim 12 < \log_{10}(L_{\rm FIR}/\mu) < 13.7$.

In comparison to existing literature, our sample exhibits [N II] line luminosity values in line with expectations, and demonstrates increasing [N II] luminosity with increasing far-infrared luminosity (see Figure 2.8) with fairly small dispersion of ~ 0.3 dex. These measurements robustly connect the comparably low (but still very luminous at $\gtrapprox 10^{12}$ $L_{\odot}$) far-infrared luminosity local (U)LIRGs to the highest and rare far-infrared luminosity sources with $\log_{10}(L_{\rm FIR}/\mu) > 13$. We calculate a fitted slope of $\alpha_{\rm SMG} \sim 0.5$ for our demagnified [N II] luminosity versus far-infrared luminosity. This is higher than the fitted slope in (U)LIRGs of $\alpha_{\rm (U)LIRGs} \sim 0.27$, indicating a key different in physical properties of the ISM.

We also investigated the $L_{[C\ II]}/L_{[N\ II]}$ ratio in the context of existing literature and their analysis. Combining our [N II] 205 μm measurements with [C II] 158 μm measurements presented in Gullberg et al. (2015), we were able to present a full distribution of $L_{[C\ II]}/L_{[N\ II]}$ in our 18 SMGs between $z = 3$ to 6. We find some of the highest and lowest $L_{[C\ II]}/L_{[N\ II]}$ values measured in high-redshift sources, and our distribution fully occupies the regions we would expect. The sample has a median value of $L_{[C\ II]}/L_{[N\ II]} \sim 12.9 \pm 4.5$, and an interquartile range of approximately 12, spanning between 10.7 and 22.6. These results are consistent with the literature, with slightly higher values compared to local (U)LIRGs which have a median value of ~ 9. Compared to other high-redshift measurements of the line luminosity ratio, we find that our sample has a lower median value than the literature's median of ~ 19. Future studies may illuminate a physical reason for this difference, as current literature sources typically are unique sources in over-dense environments, and therefore may exhibit environmental biases compared to our uniformly-selected sample of SMGs. The

$L_{[C\ II]}/L_{[N\ II]}$ doesn't show an obvious trend as a function of far-infrared luminosity in this range, despite a small increase in sources with demagnified far-infrared luminosity exceeding 10^{13} $L_{\odot}$. With dust temperature we do not detect a relationship between the [N II] 205 μm line luminosity or the $L_{[C\ II]}/L_{[N\ II]}$ ratio.

By utilizing the line ratio modelling of previous researchers such as Oberst et al. (2006); Nagao et al. (2012), we investigate the implications of the $L_{[C\ II]}/L_{[N\ II]}$ distribution we observe. We note that to disentangle the various physical parameters that affect the $L_{[C\ II]}/L_{[N\ II]}$ ratio, we need further observations such as the [N II] 122 μm line, which will help us determine gas densities. Recently, a proposal to observe the [N II] 122 μm line in 14 of our sources was accepted for ALMA Cycle 6. Overall, this sample provides the first robust characterization of the high-redshift $L_{[C\ II]}/L_{[N\ II]}$ distribution in dusty galaxies.

4.2 A narrow-band survey of high-redshift star formation

We presented a new narrow-band survey of high-redshift galaxies utilizing the infrared camera WIRCam onboard the Canada France Hawaii Telescope. The survey targets star-forming emission line galaxies by utilizing narrow-band imagery in combination with existing broad-band imagery in the same region of the sky. The CO narrow-band filter has a central wavelength of 2320 nm. This means it should pass light from the Hα λ6563, [O III] λ5007, [O III] λ4959, Hβ λ4861, and [O II] λ3727 emission lines at redshifts of $z \sim 2.53$, 3.63, 3.68, 3.77, and 5.22, respectively.

To date, the survey has observed the sky for approximately 90 hours, with 45 hours in

each of the UDS and COSMOS survey fields. Each 45 hour observation is split between a 30 hour and a 15 hour pointing, giving us two panels in each field equaling an on-sky area of approximately 0.25 $\deg^2$. Therefore to date we have a total on-sky area of approximately 0.5 $\deg^2$.

Our first results indicate detection of a number of candidates at $z \sim 2.5$ with a few candidates at $z \sim 3.6$. To date, we have no candidates at $z \sim 5.2$. A successful proposal for time with an infrared spectrometer (GNIRS) aboard the Gemini North telescope has observed approximately a dozen of these candidate galaxies, with the most significant narrow-band excess magnitudes.

The next steps in this study will be to confirm the detections of these emission lines by analyzing the GNIRS data, and leveraging this to apply for further CFHT WIRCam time to expand our on-sky survey area.

Bibliography

Alexander, D. M., Bauer, F. E., Chapman, S. C., et al. 2005, The Astrophysical Journal, 632, 736

Aravena, M., Spilker, J. S., Bethermin, M., et al. 2016, Monthly Notices of the Royal Astronomical Society, 457, 4406

Baldry, I. K., Glazebrook, K., Brinkmann, J., et al. 2004, The Astrophysical Journal, 600, 681

Barger, A. J., Cowie, L. L., & Richards, E. A. 2000, The Astronomical Journal, 119, 2092

Best, P., Smail, I., Sobral, D., et al. 2013, in Thirty Years of Astronomical Discovery with UKIRT, ed. A. Adamson, J. Davies, & I. Robson (Dordrecht: Springer Netherlands), 235–250

Béthermin, M., Breuck, C. D., Gullberg, B., et al. 2016, Astronomy & Astrophysics, 586, L7

Blain, A. W., Smail, I., Ivison, R., Kneib, J.-P., & Frayer, D. T. 2002, Physics Reports, 369, 111

Blain, A. W., Smail, I., Ivison, R. J., & Kneib, J.-P. 1999, Monthly Notices of the Royal Astronomical Society, 302, 632

Bolatto, A. D., Wolfire, M., & Leroy, A. K. 2013, Annual Review of Astronomy and Astrophysics, 51, 207

Brauher, J. R., Dale, D. A., & Helou, G. 2008, The Astrophysical Journal Supplement Series, 178, 280

Bromm, V. & Yoshida, N. 2011, Annual Review of Astronomy and Astrophysics, 49, 373

Bunker, A. J., Warren, S. J., Hewett, P. C., & Clements, D. L. 1995, Monthly Notices of the Royal Astronomical Society, 273, 513

Calanog, J. A., Wardlow, J., Fu, H., et al. 2013, The Astrophysical Journal, 775, 61

Calzetti, D., Armus, L., Bohlin, R. C., et al. 2000, The Astrophysical Journal, 533, 682

Carles, C., Martel, H., Ellison, S. L., & Kawata, D. 2016, Monthly Notices of the Royal Astronomical Society, 463, 1074

Carlstrom, J. E., Ade, P. A. R., Aird, K. A., et al. 2011, Publications of the Astronomical Society of the Pacific, 123, 568

Casali, M., Adamson, A., Alves de Oliveira, C., et al. 2007, A&A , 467, 777

Casey, C. M., Narayanan, D., & Cooray, A. 2014, Physics Reports, 541, 45 , dusty star-forming galaxies at high-redshift

Chapman, S. C., Blain, A. W., Ivison, R. J., & Smail, I. R. 2003, Nature, 422, 695 EP

Chapman, S. C., Blain, A. W., Smail, I., & Ivison, R. J. 2005, The Astrophysical Journal, 622, 772

Cirasuolo, M., McLure, R. J., Dunlop, J. S., et al. 2007, Monthly Notices of the Royal Astronomical Society, 380, 585

Conselice, C. J. 2014, Annual Review of Astronomy and Astrophysics, 52, 291

Cormier, D., Madden, S. C., Lebouteiller, V., et al. 2015, Astronomy & Astrophysics, 578, A53

Cowley, W. I., Béthermin, M., Lagos, C. d. P., et al. 2017, Monthly Notices of the Royal Astronomical Society, 467, 1231

Cucciati, O., Tresse, L., Ilbert, O., et al. 2012, Astronomy & Astrophysics, 539, A31

da Cunha, E., Walter, F., Smail, I. R., et al. 2015, The Astrophysical Journal, 806, 110

Decarli, R., Walter, F., Carilli, C., et al. 2014, The Astrophysical Journal Letters, 782, L17

Díaz-Santos, T., Armus, L., Charmandaris, V., et al. 2017, The Astrophysical Journal, 846, 32

Draine, B. 2003, Annual Review of Astronomy and Astrophysics, 41, 241

Drake, A. B., Simpson, C., Baldry, I. K., et al. 2015, Monthly Notices of the Royal Astronomical Society, 454, 2015

Dwek, E., Arendt, R. G., Hauser, M. G., et al. 1998, The Astrophysical Journal, 508, 106

Ferland, G. J., Korista, K. T., Verner, D. A., et al. 1998, Publications of the Astronomical Society of the Pacific, 110, 761

Ferland, G. J., Porter, R. L., van Hoof, P. A. M., et al. 2013, Revista Mexicana de Astronomía y Astrofísica, 49, 137

Geach, J. E., Smail, I., Best, P. N., et al. 2008, Monthly Notices of the Royal Astronomical Society, 388, 1473

Goldsmith, P. F., Yıldız, U. A., Langer, W. D., & Pineda, J. L. 2015, The Astrophysical Journal, 814, 133

Gong, Y., Cooray, A., Silva, M. B., et al. 2017, The Astrophysical Journal, 835, 273

Greve, T. R., Vieira, J. D., Weiß, A., et al. 2012, The Astrophysical Journal, 756, 101

Gullberg, B., De Breuck, C., Vieira, J. D., et al. 2015, Monthly Notices of the Royal Astronomical Society, 449, 2883

Hainline, L. J., Blain, A. W., Smail, I., et al. 2011, The Astrophysical Journal, 740, 96

Hayward, C. C. 2013, Monthly Notices of the Royal Astronomical Society: Letters, 432, L85

Herrera-Camus, R., Bolatto, A., Smith, J. D., et al. 2016, The Astrophysical Journal, 826, 175

Holland, W. S., Robson, E. I., Gear, W. K., et al. 1999, Monthly Notices of the Royal Astronomical Society, 303, 659

Iono, D., Wilson, C. D., Yun, M. S., et al. 2009, The Astrophysical Journal, 695, 1537

Ivison, R. J., Papadopoulos, P. P., Smail, I., et al. 2011, Monthly Notices of the Royal Astronomical Society, 412, 1913

Kennicutt, R. C. J. 1998, The Astrophysical Journal, 498, 541

Langer, W. D., Goldsmith, P. F., Pineda, J. L., et al. 2015, A&A, 576, A1

Lawrence, A., Warren, S. J., Almaini, O., et al. 2007, Monthly Notices of the Royal Astronomical Society, 379, 1599

Lee, G.-H., Park, C., Lee, M. G., & Choi, Y.-Y. 2012, The Astrophysical Journal, 745, 125

Lilly, S. J., Le Fevre, O., Hammer, F., & Crampton, D. 1996, ApJ , 460, L1

Lu, N., Zhao, Y., DÃaz-Santos, T., et al. 2017, ApJSS, 230, 1

Ma, J., Gonzalez, A. H., Spilker, J. S., et al. 2015, The Astrophysical Journal, 812, 88

Madau, P. & Dickinson, M. 2014, Annual Review of Astronomy and Astrophysics, 52, 415

Magnelli, B., Lutz, D., Santini, P., et al. 2012, A&A, 539, A155

Malhotra, S., Helou, G., Stacey, G., et al. 1997, The Astrophysical Journal Letters, 491, L27

McMullin, J. P., Waters, B., Schiebel, D., Young, W., & Golap, K. 2007, in Astronomical Society of the Pacific Conference Series, Vol. 376, ADASS XVI, ed. R. A. Shaw, F. Hill, & D. J. Bell, 127

Michalowski, M., Hjorth, J., & Watson, D. 2010, Astronomy & Astrophysics, 514, A67

Michalowski, M. J., Dunlop, J. S., Cirasuolo, M., et al. 2012, Astronomy & Astrophysics, 541, A85

Mocanu, L. M., Crawford, T. M., Vieira, J. D., et al. 2013, The Astrophysical Journal, 779, 61

Nagao, T., Maiolino, R., De Breuck, C., et al. 2012, Astronomy & Astrophysics, 542, L34

Narayanan, D., Turk, M., Feldmann, R., et al. 2015, Nature, 525, 496 EP

Noll, S., Burgarella, D., Giovannoli, E., et al. 2009, Astronomy and Astrophysics, 507, 1793

Oberst, T. E., Parshley, S. C., Stacey, G. J., et al. 2006, The Astrophysical Journal Letters, 652, L125

Pavesi, R., Riechers, D. A., Capak, P. L., et al. 2016, The Astrophysical Journal, 832, 151

Pohlen, M., Cortese, L., Smith, M. W. L., et al. 2010, Astronomy & Astrophysics, 518, L72

Puget, P., Stadler, E., Doyon, R., et al. 2004, in Proc. SPIE , Vol. 5492, Ground-based Instrumentation for Astronomy, ed. A. F. M. Moorwood & M. Iye, 978–987

Rawle, T. D., Egami, E., Bussmann, R. S., et al. 2014, The Astrophysical Journal, 783, 59

Riechers, D. A., Carilli, C. L., Capak, P. L., et al. 2014, The Astrophysical Journal, 796, 84

Smail, I., Chapman, S. C., Blain, A. W., & Ivison, R. J. 2004, The Astrophysical Journal, 616, 71

Sobral, D., Matthee, J., Best, P. N., et al. 2015, Monthly Notices of the Royal Astronomical Society, 451, 2303

Sparke, L. & Gallagher, J. 2000, Galaxies in the Universe: An Introduction (Cambridge University Press)

Spilker, J. S., Marrone, D. P., Aravena, M., et al. 2016, The Astrophysical Journal, 826, 112

Stacey, G. J., Geis, N., Genzel, R., et al. 1991, The Astrophysical Journal, 373, 423

Stacey, G. J., Hailey-Dunsheath, S., Ferkinhoff, C., et al. 2010, The Astrophysical Journal, 724, 957

Strandet, M. L., Weiss, A., Breuck, C. D., et al. 2017, The Astrophysical Journal Letters, 842, L15

Strandet, M. L., Weiss, A., Vieira, J. D., et al. 2016, The Astrophysical Journal, 822, 80

Swinbank, A. M., Simpson, J. M., Smail, I., et al. 2014, Monthly Notices of the Royal Astronomical Society, 438, 1267

Tacconi, L. J., Genzel, R., Smail, I., et al. 2008, The Astrophysical Journal, 680, 246

Tayal, S. S. 2011, The Astrophysical Journal Supplement Series, 195, 12

Toft, S., Smolčíc, V., Magnelli, B., et al. 2014, The Astrophysical Journal, 782, 68

Umehata, H., Matsuda, Y., Tamura, Y., et al. 2017, The Astrophysical Journal Letters, 834, L16

Vieira, J. D., Crawford, T. M., Switzer, E. R., et al. 2010, The Astrophysical Journal, 719, 763

Vieira, J. D., Marrone, D. P., Chapman, S. C., et al. 2013, Nature, 495, 344 EP

Wang, L., Gonzalez-Perez, V., Xie, L., et al. 2017, Monthly Notices of the Royal Astronomical Society, 468, 4579

Wang, S. X., Brandt, W. N., Luo, B., et al. 2013, The Astrophysical Journal, 778, 179

Wardlow, J. L., Smail, I., Coppin, K. E. K., et al. 2011, Monthly Notices of the Royal Astronomical Society, 415, 1479

Watson, D. M. & Storey, J. W. V. 1980, International Journal of Infrared and Millimeter Waves, 1, 609

Weiß, A., Breuck, C. D., Marrone, D. P., et al. 2013, The Astrophysical Journal, 767, 88

Yuma, S., Ouchi, M., Drake, A. B., et al. 2017, The Astrophysical Journal, 841, 93

Zhao, Y., Lu, N., Xu, C. K., et al. 2013, The Astrophysical Journal Letters, 765, L13

Zhao, Y., Lu, N., Xu, C. K., et al. 2016, The Astrophysical Journal, 819, 69